Alma Mater Studiorum - University of Bologna

SCHOOL OF SCIENCE

Department of Industrial Chemistry"Toso Montanari"

Master Degree in

Low carbon technologies and sustainable chemistry

(LOCATE)

Class LM-75 - Environmental and land sciences

Optimization of aqueous Zn-ion batteries

Experimental Thesis

CANDIDATE

Maedeh Askarzadehardestani

SUPERVISOR

Marco Giorgetti

CO-SUPERVISOR

Min Li

Mariam Maisuradze

Second Session of October

Academic Year 2021-2022

Contents

List of figures:

List of tables:

Abstract

MnHCF was synthesized by simple co-precipitation method. In this work we investigate the electrochemical behavior of manganese hexacyanoferrate in zinc sulfate ($ZnSO_4$), $ZnSO_4$+$MnSO_4$ and zinc triflate ($Zn(OTF)_2$) aqueous electrolytes. Electrochemical tests were performed by both El-cell which is designed for reflection investigation and coin cell. In cyclic voltammetry curves,we observed redox peaks of both $Fe^{3+/2+}$ and $Mn^{3+/2+}$ pairs. The results based on current shows that the capacity of battery is controlled by diffusion process in aqueous electrolyte system. MnHCF undergoes severe dissolution and zinc displacement during cycling. Compared to $ZnSO_4$, anions of Zn $(OTF)_2$ electrolyte are strongly adsorbed on the electrolyte surface, in turn hindering the water oxidation reaction and reducing the decomposition of MnHCF. The MnHCF/Zn battery using 3M Zn $(OTF)_2$ delivers a specific capacity of 41 $mAhg^{-1}$ at 50 mAg^{-1} while by using 3M $ZnSO_4$+1M $MnSO_4$ the specific capacity reaches to 400 $mAhg^{-1}$ for the pure sample and around 250 $mAhg^{-1}$ for the MnHCF+A. Our results suggest that the anions in the aqueous electrolyte are of great importance to optimize the electrochemical performance of metal hexacyanoferrates.

The pre-addition of $MnSO_4$ into $ZnSO_4$ solution is capable of easing the Mn^{2+} dissolution from the cathode.

1.Introduction

1.1 Study background

As the world's population has grown and per capita energy consumption and the, global energy consumption has increased rapidly. The impact of this growing energy consumption on the environment and society is becoming increasingly apparent. This has accelerated the development and deployment of renewable energy technologies and facilities (RES). Meanwhile, the rise of RES has highlighted the next major challenge: storing energy when demand is less than supply. There are several energy storage technologies, many of which have been in use for decades, as shown in Figure 1 [1]. Among the various technologies, pumped storage and compressed air storage are widely used, but both have significant infrastructure requirements that limit large-scale energy storage to specific locations [2]. Batteries currently have the greatest potential to reduce costs. And rechargeable lithium-ion batteries (LIBs) are the leading option for this application.

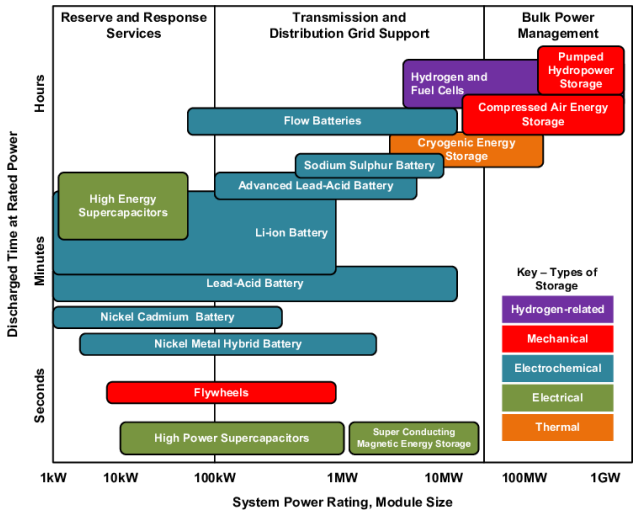

Figure 1. Applicable power ranges and discharge power duration of different energy storage technologies

Unlike “primary” lithium batteries, “secondary” lithium-ion batteries (LIBs) are rechargeable. LIBs were proposed by British chemist M. Stanley Whittingham in the 1970s [3] and first cyanoligands by Sony in 1991 [4]. Li-ion batteries are widely used in portable electronic devices and power tools due to their high energy density and efficiency among practical secondary batteries. In 2011, Li-ion batteries accounted for 66% of all portable secondary batteries sold in Japan [5]. The next targets for LIBs are considered to be automotive applications and extremely large energy storage systems. The technology of Li-ion batteries is based on the displacement of lithium ions between positive and negative electrodes during charging and discharging, which is why the Li-ion battery is also known as the “rocking chair battery”. The most commonly used electrode material for Li-ion battery is lithium cobalt oxide ($LiCoO_2$), which offers high energy density but presents safety risks, especially when damaged, also has high cost and its resources is limited. Lithium iron phosphate ($LiFePO_4$), lithium ion manganese oxide battery ($LiMn_2O_4$, $LiMnO_3$, or LMO), and lithium nickel manganese cobalt oxide offer lower energy density but longer lives and less likelihood of fire or explosion [6,7]. Meanwhile, another concerning issue is lithium resources, because the lithium resources are limited, and the cost of lithium-based raw materials has roughly doubled from the first practical application in 1991 till now, and it will increase more as the demand for lithium rises with the large-scale commercialization of LIBs [8,9].

For stationary applications of cells, the most important parameters to consider are price ($\$ W h^{-1} kg^{-1}$), lifetime (years, cycle number), power density ($W kg^{-1}$), and safety. This requires raw materials that are abundant (low price). For this reason, the greater availability and accessibility of alkali metals (Na^+, K^+) and alkaline earth metals (Mg^{2+}) compared to lithium encourages the study of Na-ion, K-ion, and Mg-ion batteries. The use of Li metal anodes leads to serious safety issues related to the growth of Li dendrites during battery cycling. Therefore, some dendrite-free metals (K, Mg, etc.) are the ideal anode material. Meanwhile, all alkali metal ions (Li^+/ Na^+/ K^+) have a similar tendency to lose electrons. As shown in Table 1, the potential of Na^+/Na is -2.71 V (0.3V higher than Li^+/Li -3.04 V), and the difference between K^+ /K (- 2.93 V) and Li^+/Li is only 0.11 V [10-11]. So it is obvious to shift the research focus to non-Li ion systems,

because most of the research experiences and well-developed electrodes of LIBs can be directly applied to the non-Li ion batteries.

The technology of sodium and potassium Ion batteries has recently attracted a lot of attention in the scientific community because of the abundance and accessibility of alkali metals (Na^+, K^+), making them a viable and more environmentally friendly alternative to Li-ions. Because of the similar tendency to lose electrons and the relatively small potential difference (-2.924 V vs SHE for potassium; -2.711 V vs. SHE for sodium), alkali metals may be a viable option for developing new systems without using Li-ions. The possibility of using the same research experience as well as the developments in Li-ion battery electrodes for new alkali ion batteries can be considered as one of the main advantages of these materials.

Table 1. Potential and atomic/ion radius of alkali/ alkaline-earth metal

Alkali/alkaline-earth metal	Potential (V vs SHE)	Potential (V vs Li^+/Li)	Atomic radius (Å)	Ionic radius (Å)	Hydrated ion radius (Å)
Li^+/Li	-3.04	0	1.34	0.76	2,37
Na^+/Na	-2.71	0.3	1.54	1.02	1,83
K^+/K	-2.93	0.11	1.96	1.38	1,38
Be^{2+}/Be	-1.85	1.19	1.12	0.27	4,08
Mg^{2+}/Mg	-2.36	0.68	1.45	0.72	3,46
Ca^{2+}/Ca	-2.87	0.17	1.94	1.06	3,09
Sr^{2+}/Sr	-2.89	0.15	2.19	1.18	3,09
Al^{3+}/Al	-1.66	1.38	1,18	0,68	-

1.2 Types of cathodes

1.2.1 Manganese-based materials:

Zn^{2+} ions, with a small radius of 0.75 A°, are proposed to be able to be successfully transported along large crystal tunnels. Manganese oxides with multiple valence states show a variety of crystal structures, in which manganese dioxide has the most abundant structures, including α-, β-, γ-, λ-, δ-, and R-types (Fig. 2) [12]. The basic crystal structure of manganese dioxide is an octahedral unit composed of six oxygen atoms and one manganese atom. The MnO_6 octahedral units are interconnected to form a tunnel structure, which size is determined by the number of MnO_6 octahedrons; while, α-MnO_2 manifests a large [2 × 2] tunnel structure along the c-axis with four edge-sharing MnO_6 octahedral units(Fig. 2a); β-MnO_2 grows along the c-axis to form [1 × 1] tunnels (Fig. 2b); todorokite MnO_2 has larger [3 × 3] tunnels with a similar structure of α -MnO_2 (Fig. 2d) and γ-MnO_2 features [1 × 1] and [1 × 2] hybrid tunnels along the β -axis (Fig. 2f); δ-MnO_2 presents a layered structure with large interlayer spacing (7 Å) (Fig. 2e), and λ-MnO_2 is a spinel structure (Fig. 2c). The diverse crystal structures result in differences in the electro- chemical performance, and manganese oxides with larger tunnels have a faster ion-diffusion capacity [13,14].

From the point of view of the crystal structure, α-MnO_2 (2 × 2 tunnels, 4.6 Å), the layered structure δ-MnO_2 (interlayer spacing 7 Å), and γ-MnO_2 are comprised of randomly arranged layers (1 × 1, 2.3 × 2.3 Å and 1 × 2, 2.3 × 4.6 Å), which makes them amenable to the insertion of Zn^{2+}, and consequently, a variety of scientific investigations have been performed and proved their successful utilization as high-performance aqueous ZIBs cathodes [14-17]. However, β-MnO2 is intrinsically unfavorable for the storage of numerous Zn^{2+} ions due to its narrow 1 × 1 tunnels structure [14-16]. Preparing β-MnO_2 with a unique morphology can serve as an effective approach to tailor its electrochemical performance [18]. Although todorokite MnO_2 has large [3 × 3] tunnels, its tunnels are already occupied by a number of Mg^{2+}, which affects the average oxidation state of the manganese [13]. Therefore, the theoretical cathodic capacity of todorokite MnO_2 was calculated to be 99 mA h g^{-1}, equivalent to only 40% of α-MnO_2. The acid treatment of todorokite MnO_2 can remove the Mg^{2+} from the

tunnels [19], which may effectively change the oxidation state of the manganese, leading to a higher discharge capacity. Spinel-type λ-MnO_2 and $ZnMn_2O_4$ may not be desirable materials for Zn^{2+} insertion because of their limited 3D tunnels. The high electrostatic interaction among the Zn^{2+} ions and the $ZnMn_2O_4$ lattice (Fig. 2h) contribute to the difficulty of Zn^{2+} intercalation [20]. The introduction of cation deficiencies into the $ZnMn_2O_4$ lattice was suggested to lower the electrostatic barrier and facilitate Zn^{2+} diffusion in the host (Fig. 3a and b) [21]. In view of making cation defects, extracting oxygen anions from the $ZnMn_2O_4$ cathode could increase the electrostatic repulsion among Zn^{2+} ions within the lattice, which will favor the fast extraction of Zn^{2+} from $ZnMn_2O_4$ to form Zn vacancies.

The results of the experimental measurements combined with density functional theory (DFT) studies suggested that the oxygen defects in $ZnMn_2O_4$ were capable of tailoring the electronic conductivity, Zn^{2+} diffusion kinetics, Zn vacancy formation energy, and the energy barrier of Zn mobility [22]. Other types of manganese-based materials have also been reported to have the ability to allow the insertion of Zn^{2+}, including MnO_2-birnessite, [23], MnO[24], Mn_2O_3 [25], Mn_3O_4 [26,27], $MgMn_2O_4$[28].

While attractive in terms of high capacity and high energy density, manganese-based materials still suffer from limitations in their electrochemical performance resulting from their low intrinsic electronic conductivity and the inevitable Mn dissolution, which directly cause a poor rate capability and rapid capacity fading.

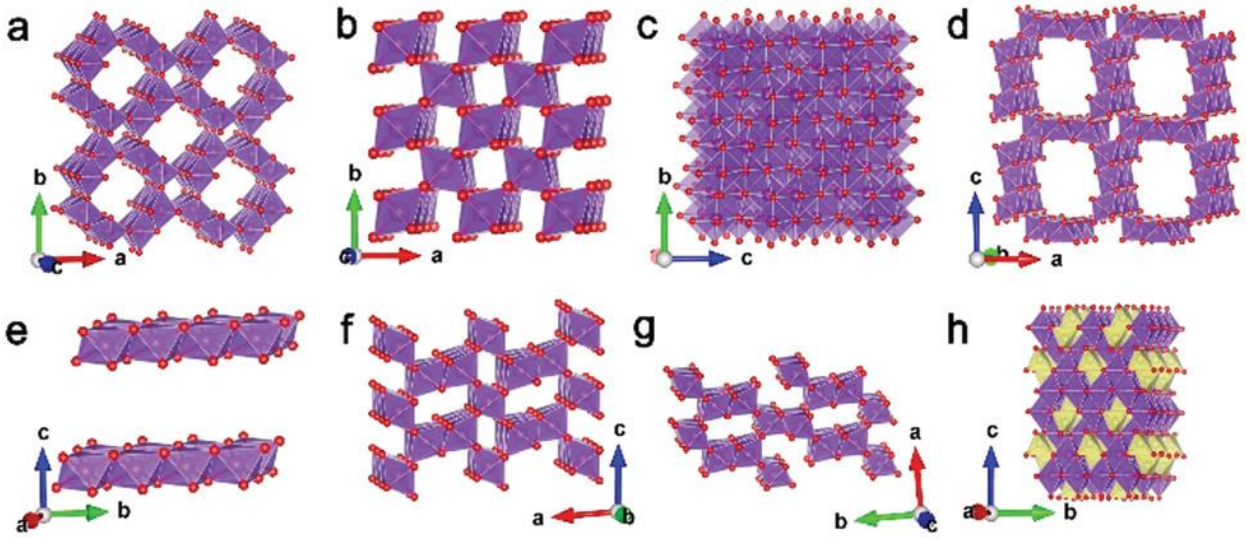

Figure 2. Schematic diagram of various crystal structures of manganese based materials: (a) α-MnO_2; (b) β-MnO_2; (c) λ-MnO_2; (d) todorokite MnO_2; (e) δ-MnO_2; (f) γ-MnO_2; (g) R-MnO_2; (h) $ZnMn_2O_4$.

1.2.2 Vanadium-based materials:

Vanadium-based materials, especially vanadium oxides, possess a large-tunnel framework, which present the possibility to accommodate numerous Zn^{2+}-ions for storage [29]. The electrochemical performance of vanadium-based materials was suggested to be mainly governed by their geometric structures. For example, V_2O_5 suffers from low capacity and instability with the repeated intercalation of ions, especially multivalent ions, due to its unstable single layer structure and pure +5 valence of V (Fig. 3d) [30,31]. The inferior performance of V_2O_5 has led to increased interests in exploring vanadium oxides with more stable structures to mitigate the capacity fading issue. Compared to V_2O_5, VO_2 with a tunnel-like framework (Fig. 3e) possesses a remarkable ability for rapid Zn^{2+} (de)intercalation, demonstrating excellent rate performance as an aqueous ZIBs cathode [32]. Tunnel-like V_6O_{13}, apart from providing mixed vanadium states of V^{4+}/V^{5+}, is comprised of alternant single and double vanadium oxide layers, which offer more active sites for ions storage (Fig. 3f). A high capacity of 5 A g^{-1} was reported for V_6O_{13} as an aqueous ZIBs cathode (295 mA h g^{-1} after 1000 cycles) (Fig. 3g) and a capacity of 206 mAh g^{-1} could be maintained after

3000 cycles at 10 Ag^{-1}[33]. The electrochemical performance of V_2O_5 could be improved by making mixed vanadium valences. The presence of V^{4+} leads to higher electrochemical activity, lower polarization, faster ion diffusion, and higher electrical conductivity than pure V_2O_5 without V^{4+} [34].

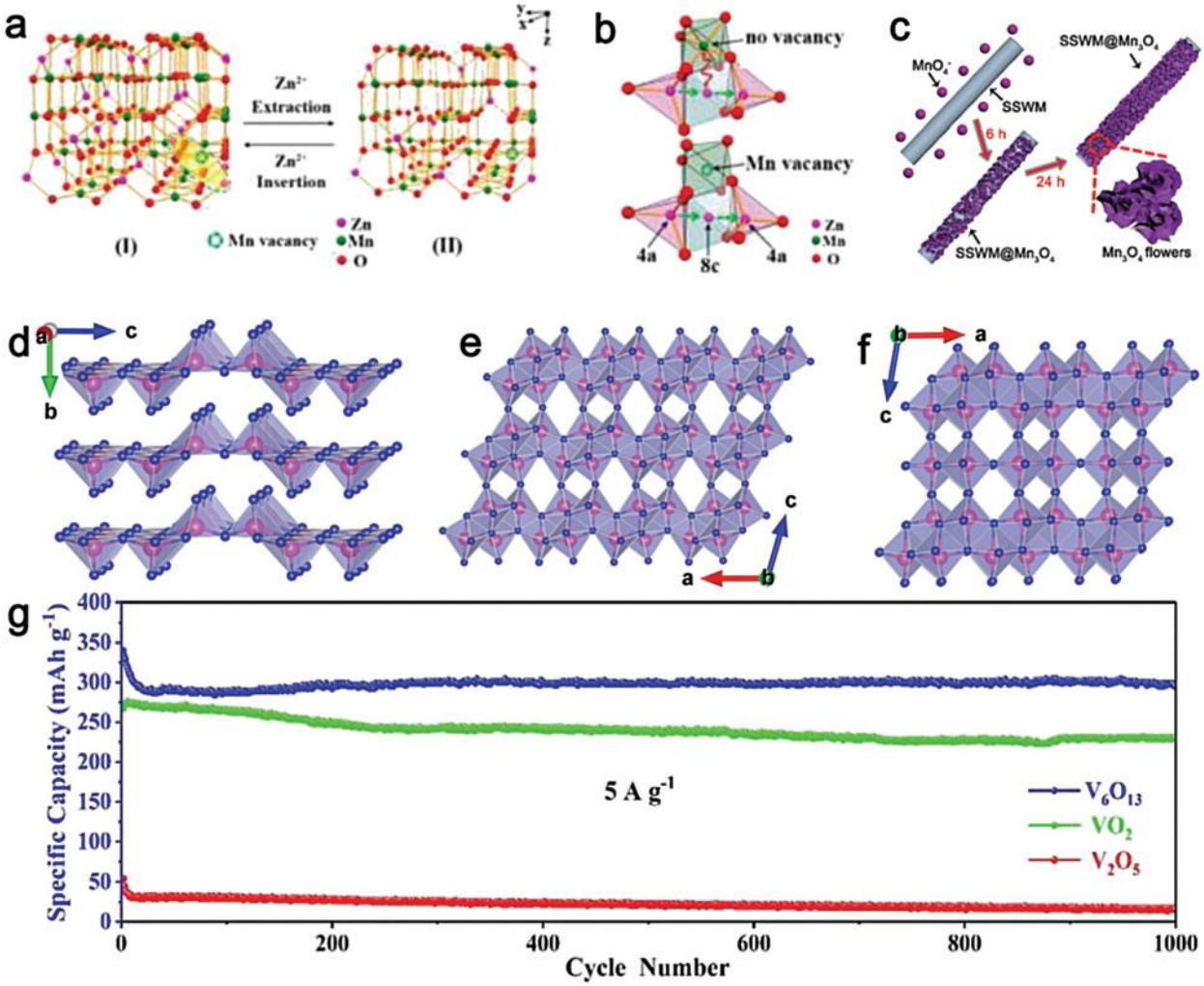

Figure 3: Structural illustrations of Zn^{2+} that it's a insertion/extraction in a $ZnMn_2O_4$ spinel with Mn vacancies and (b) crystal structure of a $ZnMn_2O_4$ spinel without and with Mn vacancies (c) Synthesis illustration of SSWM@Mn_3O_4 (d–f) Schematic diagram of various crystal structures of V_2O_5, VO_2, and V_6O_{13}. (g) Long-term cycling performance of V_2O_5, VO_2, and V_6O_{13} at current densities of 5 A g^{-1}

1.2.3 Prussian Blue analogues:

A new class of electrodes made of active material are structures with open frameworks, such as the analogues of Prussian blue. Prussian blue, also called iron (III) ferrocyanide Fe^{III} $[Fe^{II}(CN)_6]$, originally Berlin blue, was first and accidentally discovered by Heinrinch Diesbach in 1704 and found use not only as a blue pigment and substitute for the much more expensive lapis lazuli, but also as an antidote. It consists of an open framework that served to irreversibly trap the thallium(I) ion, which could return the potassium ion originating from the reactants to the interstitial space [35]. This property, known as ion exchange, is nowadays used to trap cesium-137 from waste streams in nuclear fuel processing [36]. It is necessary to distinguish between the soluble and insoluble forms of Prussian blue, and these terms do not refer to the actual solubility, but to the tendency to form a colloidal solution or not, which is due to the absence or presence of vacancies and interstices[37].

Prussian blue analogues (PBAs) are bimetallic cyanides with a three-dimensional lattice of repeating units of -NC-Fe-CN-M-NC-, where M denotes a transition metal, generally Mn, Co, Ni, Cu, Zn [38]. Since iron is usually present, these compounds are called hexacyanoferrates, otherwise, when iron is not present, they are simply called hexacyano-metallates. Many papers have been written on PBAs, for example, on the electrochemical detection of hydrogen peroxide [39].

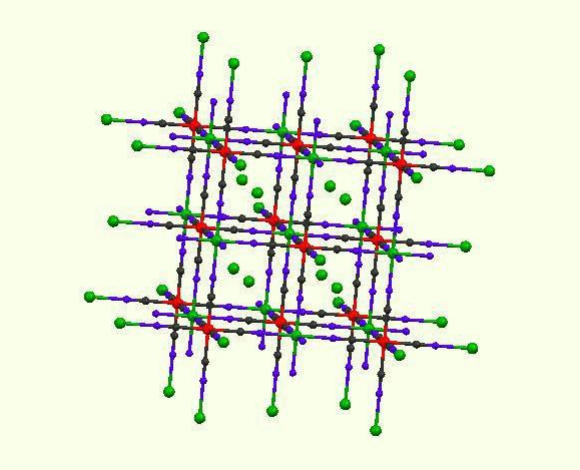

Figure 4. Structure of a metal hexacyanoferrate[40]

The cyanoligands act as a bridge between Fe and M, connecting them in a precise manner, with the carbon bonded to Fe while the nitrogen is bonded to M (Figure 4). Moreover, due to the strong-field ligand, iron is usually present as Fe (III) in a low-spin state, while M is a divalent ion. A change in the oxidation state of M from (+2) to (+3), which is meanwhile compensated by interstitial ions, leads to a contraction of cell dimensions, generally by 10 A˚ [41]. Both Fe and M can behave as redox centers (as demonstrated by their electrocatalytic properties [41]), so the resulting capacitance can be higher than for electrodes where only one metal undergoes a redox reaction.

Due to the three-dimensional lattice, Prussian blue analogues are even characterized by flexibility, which is due to the stretching of the cyanoligands, which also have the function of mediating metal-to-metal charge transfer [42]. In fact, the C-terminus is able to remove charge through a π-bond and place it at the N-terminus, allowing the interaction between the generally 5A˚removed metals, thus giving rise to magnetic and optical properties [43].

As for the porous structure, the open framework is given by repeated cavities of the octahedral unit $[M(CN)_6]$. These cavities contain both coordinated and weakly bound water, which can be removed below 100°C without changing the existing structure [43]. Moreover, due to the large interstices and channels, these compounds can accommodate both Li and Na ions, which are thus prepared for use in batteries. Even Al ions have been successfully inserted and extracted [44].

PB follows different changes of its chemical composition with no breaking the whole crystal structure of the system. Substitutional and interstitial changes of PB causes to a series of new compounds which are called Prussian blue analogues (PBAs). When we substitute Fe sites with other metals, such as Zn, Cu, Ni, Mn, Co, V, In etc. [93-95], we get a series of bimetallic cyanide Fe -C-N-M with same structure of PB. The crystal structure of PBAs is illustrated in figure 5. Recently, these types of compounds have gained popularity not only because of their ability to accommodate ions or even small molecules, e.g. hydrogen, but also because of their cheap price and ease of synthesis.

The chemical formula of PBA can be expressed as $A_xM_y[M(CN)_6]\cdot nH_2O$, where A denotes an alkali metal such as Li^+/ Na^+/ K^+, etc.; M' represents transition metal ions such as Fe, Mn, Co, Ni, Mn, Cu, etc.; $0<x<2$; $0<y<1$. The benefits of PBA as ideal

insertion/electrode material are illustrated in following:

(i) 3D scaffold and opened ion channel. Like PB, PBAs also generally exhibit a cubic lattice,and the M' and M ions are sixfold (octahedral) coordinated to the carbon and nitrogen atoms of the CN ligands, forming a rigid 3D scaffold with open ion channels and spacious interstitial spaces. In contrast to conventional insertion compounds of transition metal oxides and phosphates, PB lattices have large interstitial sites (≈4.6 Å diameter) and spacious channels (3.2 Å diameter in < 100 > direction), resulting in a high diffusion coefficient of 10^{-9} to 10^{-8} cm^2s^{-1} [45, 46,47], implying much higher ionic conduction in the PB lattice than in the conventional insertion cathode of oxide and phosphate.

ii) Two different redox active centers. PBA compounds contain two distinct redox active centers: $M'^{2+/3+}$ and $M^{2+/3+}$ (usually M=$Fe^{2+/3+}$) pairs, both of which can undergo a full electrochemical redox reaction (when M'=Fe, Co, Mn, etc.) and contribute a capacity for two-electron transfer through a reversible insertion/extraction reaction process.

$A_2\ M'^{II}\ [Fe^{II}\ (CN)_6] \leftrightarrow A\ M'^{III}\ [Fe^{II}\ (CN)_6] + A + e^-$

$A\ M'^{III}\ [Fe^{II}\ (CN)_6] \leftrightarrow M'^{III}\ [Fe^{III}\ (CN)_6] + A + e^-$

(iii)The Fe site within the PB compound can be partially or completely replaced by many redox-active transition metals without damaging the crystal structure. This complete combinability allows the electrochemical response of the PB framework to be conveniently tuned. For example, Na_2FeFe-PB exhibits charge/discharge plateaus around 3.2 V (vs. Na/Na^+) [48], while Na_2MnFe-PBA and Na_2CoFe-PBA provide much higher voltages of 3.6 and 3.8 V, respectively [49,50]. Element substitution can be used to develop PB cathodes with high capacitance. When the Fe element is completely replaced by Mn, the resulting Na_2MnMn-PBA material can provide a greatly increased Na insertion capacity of > 200 $mAhg^{-1}$ [51]. Therefore, thanks to the tunable compositions, the electrochemical properties of the PBA frameworks can be tailored to meet the requirements of the battery application.

(iv)The PBA lattice is structurally and dimensionally stable during the gas

ion insertion and removal process. As demonstrated by Cui Yi et al, CuHCF can be cycled very well at 17C for 40,000 cycles, retaining 83% of the original capacity [52].

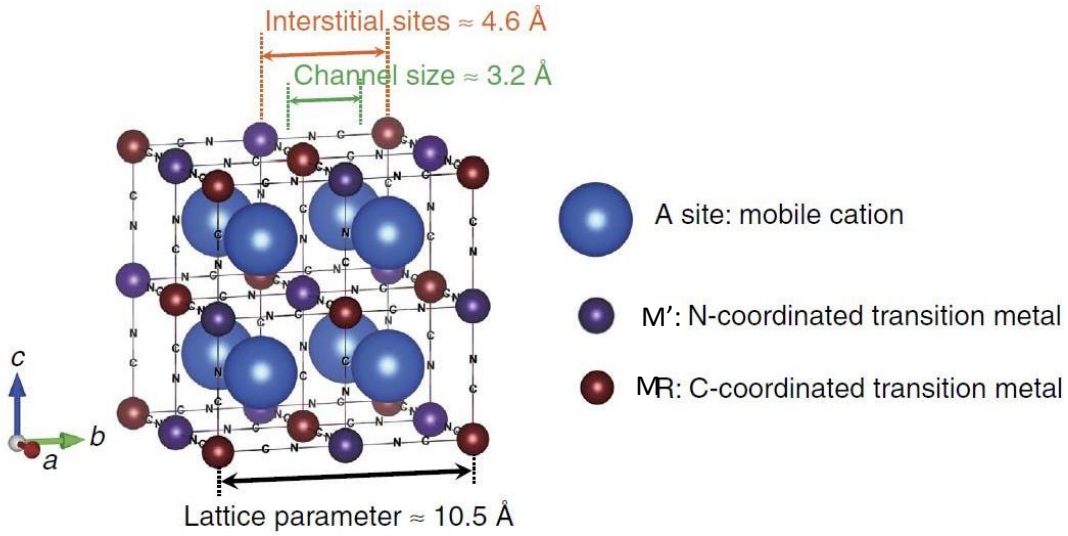

Figure 5. structure of PBA $A_xM'_y[M(CN)_6]\ nH_2O$. Cations A and water are accommodated in A-sites. M' and M are transition metal ions [47]

Among all PBAs, copper/nickel/manganese/vanadium/cobalt/chromium hexacyanoferrate (HCF) has been extensively studied in electrochemical reactions. Some literatures reported that both metal sites can be electroactive, such as $Fe^{III/\ II}$ [53], $Cu^{II/I}$ [54,55], $Mn^{III/\ II}$ [32], but in some cases only one active species $[Fe^{III/\ II}(CN)_6]^{3-/4-}$ was found to be common in the battery community [56]. However, the electroactivity of copper in a copper hexacyanoferrate-based electrode in a battery system was recently revealed by an operando XAS experiment [57]. Through work in my laboratory, we found that not only the metal sites but also the ligands are able to participate in the redox processes [58]. The complexity of batteries, consisting of different components and different contributions to the overall process, can sometimes only be untangled by a combination of complementary multitechnical approaches

The main disadvantage of Prussian Blue analogue materials is their low crystal density (1.96 g $cm^{-3}$for defect-free sodium iron hexacyanoferrate), which two times less that of high-performing lithium-ion cathodes. For this reason, PBA batteries are unlikely candidates for use in consumer electronics or electric vehicles [59-61]. Also, at a high concentration, the lattice cooperatively can be displaced in the direction, transforming

to rhombohedral geometry (Figure 6). This change in structure can lead to decrease in ionic conductivity and reversibility, lowering rate capability and cycle life, respectively. So, considerable attention should be done to the benefits of high capacity in lithium- and sodium-ion electrodes which must be accurately weighed against sacrificing to these other performance metrics [59].

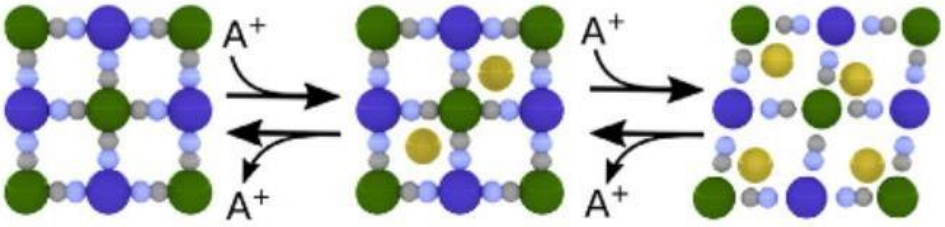

Figure 6. Insertion of alkali ions at critical concentrations can distort the structure to a less symmetric rhombohedral geometry [59]

1.3.Manganese Hexacyanoferrate (MnHCF)

Manganese hexacyanoferrate is one of the promising cathode materials for sodium ion batteries. Compared with other PBAs, MnHCF has several advantages: 1) it consists of only abundant metals, resulting in a relatively low price for the finished battery; 2) it has a large reversible specific capacity (> 120 mAh g^{-1}) and high potentials for alkali ion (K^+,Li^+,Na^+) storage [62]. Takachi et al. reported the structural, electronic and electrochemical properties of $Na_{1,32}Mn^{II}[FeII(CN)_6]_{0.833}*5H_2O$ thin film electrodes with an observed discharge capacity of 135 mAh/g due to Mn^{3+}/Mn^{2+} reduction at 3.7 V and Fe^{3+}/Fe^{2+} reduction at 3.3 V [63]. The drawback of the synthesized compound is the well-known Jahn-Teller effect, which occurs in all Mn-based trivalent materials and leads to instability of the Mn^{3+} ion, which hinders the manganese reduction reaction at high rate [64].

In general, there are three possible structures of $Na_xMn[Fe(CN)_6]$: rhombohedral, monoclinic, and cubic. The first two show poor cycling stability due to the numerous phase transitions and structural changes during Na^+ insertion/extraction. For example,

J. B. Goodenough and reported that rhombohedral $Na_xMnFe(CN)_6$ exhibit a rapid decrease in capacitance due to a phase transition from rhombohedral to cubic during Na^+ ion incorporation and removal. As for the monoclinic $Na_{1.89}Mn[Fe(CN)_6]_{0.97}$-$1.87H_2O$, it undergoes a complicated series of phase transformations (monoclinic – cubic – tetragonal) during the initial charging process [65-67]. These structural changes lead to poor cycling stability and low initial coulombic efficiency. In contrast to rhombohedral and monoclinic phases, cubic sodium manganese hexacyanoferrate exhibits high structural symmetry, which should lead to higher structural stability in sodium intercalation/extraction processes. However, to date, the cubic $Na_xMnFe(CN)_6$ is rarely used as a cathode material for sodium-ion batteries because cooperative sodium shift along the [111] axis at higher sodium concentration changes the crystal symmetry to a distorted rhombohedral or monoclinic phase [67]. Y, Tang and co-workers found that cubic and monoclinic structured $NaxMnFe(CN)_6$ synthesized with the addition of citric acid exhibited completely different cyclic stability. It has been reported that $Na_xMnFe(CN)_6$ with cubic structure can maintain the cubic phase throughout the Na^+ insertion/extraction process, while $Na_xMnFe(CN)_6$ with monoclinic structure undergoes undesirable changes throughout the cycle, leading to appreciable lattice distortions and mechanical stresses. As a result, cubic-structured manganese hexacyanoferrate exhibits a high capacity of ≈120 mAh g^{-1} and excellent cycling stability of ≈70% capacity retention over 500 cycles at 200 mA g^{-1}, compared to monoclinic-structured manganese hexacyanoferrate with only 38% capacity retention [68].

Recently, many studies have focused on improving the performance of MnHCF and other PBAs as cathode materials [69]

1.4 Aqueous rechargeable metal-ion batteries (ARMBs)

Because of their low cost, safety, environmental friendliness, and strong ionic conductivity, aqueous rechargeable metal ion batteries (ARMBs) offer enormous potential in large-scale energy storage. A variety of ARMBs have been investigated thus far, including naturally occurring alkali metal ions (Na+ and K+), also multivalent charge carriers (Zn^{2+}, $Mg^{2+,}$ Al^{3+}, etc.) [71–78]. Because of the unique properties of metallic zinc, which is an ideal anode material with high theoretical gravimetric and volumetric capacity of 820 mAh g-1 and 5855 mAh cm3, low electrochemical potential (0.76 V vs. SHE), high abundance, and intrinsic safety [79,80], aqueous Zinc-ion batteries (ZIBs) are considered some of the most promising candidates for stationary application among different ARMBs. Meanwhile, in mildly acidic aqueous solutions, stripping-plating of Zn metal anodes displays good reversibility [81].

1.5 Electrolyte optimization for more reliable aqueous ZIBs

In addition to the exploration of Zn anodes, recently, growing research efforts have been devoted to investigate the ingredient, concentration, and additives toward electrolytes in aqueous ZIBs chemistry. The modification of the electrolyte is of great significance in not only suppressing the generation of Zn dendrites but also alleviating the dissolution of cathode materials.

1.5.1 Pre-addition of relevant salts:

The pre-addition of $MnSO_4$ into $ZnSO_4$ solution is capable of easing the Mn^{2+} dissolution from the cathode [15,28]. In aqueous Zn/NaV_3O_8-1.5H_2O batteries, by adding Na_2SO_4 into $ZnSO_4$ electrolyte, for one thing, Na^+ ions with a low reduction potential are able to generate an electrostatic shield with positive charge, thus effectively inhibiting Zn dendrites, and for another, such a Na_2SO_4 additive could alleviate the dissolution of NaV_3O_8-1.5H_2O material (Fig. 7a) [82]. The addition of sodium salt into the electrolyte also exerts a positive effect on the cycling stability of an aqueous CuHCF–Zn battery. With the presence of Na^+, the high potential plateau of CuHCF was delayed and the phase transformation was slowed down[83].

1.5.2 Concentration modulation:

The fabrication of an ultraconcentrated electrolyte poses another possibility for electrolyte modulation. For example, Wang's group investigated the application of a hybrid 20M LiTFSI/1MZn $(TFSI)_2$ electrolyte, which unique properties enabled a dendrite-free Zn transportation process with about 100% coulombic efficiency as well as the suppression of water consumption. In this electrolyte, the huge amount of $TFSI^-$ anions instead of H_2O molecules preferentially bonded with Zn^{2+} ions to generate $(Zn\text{-}TFSI)^+$, meanwhile suppressing the formation of $(Zn\text{-}(H_2O)_6)^{2+}$·[84]. Moreover, the application of 30 M $ZnCl_2$ as the electrolyte demonstrated enhanced coulombic efficiency and relieved the side reactions as compared to those in dilute $ZnCl_2$ solution (Fig. 7b). This could be explained by there existing ionic species, like $[Zn(OH_2)_6]^{2+}$ and $[Zn(OH_2)_2Cl_4]^{2-}$, in $ZnCl_2$ solution, whereas, in the 30 M $ZnCl_2$ electrolyte, there were less water molecules for Zn^{2+} to form an octahedral coordination, which led to a reduction in $[Zn(OH_2)_6]^{2+}$ and $[Zn(OH_2)_2Cl_4]^{2-}$. Nevertheless, more $[ZnCl_4]^{2-}$ occurred, thus greatly inhibiting the generation of electrochemically inactive byproducts of both Zn $(OH)_2$ and ZnO [85]. This kind of high-concentrated ''water-in salt'' electrolyte is beneficial to fully understanding the aqueous ZIBs system and provides new insights for battery optimization.

1.5.3 Combination of organic/aqueous solvents:

Due to the significance of zinc electrode position efficiency for enhancing the long-term performance of aqueous zinc-ion batteries, to improve the efficiency of electrodeposition, the morphology and reactivity of the zinc deposit are also key issues. Metallic Zn demonstrates a higher thermodynamics and more simplified electrochemistry in organic solvents than in aqueous solvents, thus the side reactions could be effectively suppressed if we combine organic/aqueous solvents in aqueous ZIBs, which would make it possible to improve the coulombic efficiency as well as to minimize Zn dendrite growth and passivation. The incorporation of branched polyethyleneimine (BPEI) in $ZnSO_4$ solution suppresses the kinetics of zinc electrode position and decreases the grain growth rate. The BPEI will adsorb on the surface of the substrate to favor Zn nucleation over the growth, which facilities a homogeneous distribution of the current densities and the uniformity of the deposited layer [86]. The

use of triethyl phosphate (TEP) co-solvent in the aqueous electrolyte induces mainly the deposition of $Zn_3(PO_4)_2$ on the Zn anode surface instead of ZnO. $Zn_3(PO_4)_2$ could function as a molecular template for Zn nucleation, resulting in porous structures. Therefore, the dendrite would be effectively suppressed and a remarkable cycling behavior for over 3000 h could be achieved [87]. The polyacrylamide (PAM) electrolyte additive can absorb on the surface of Zn anode, which is an effective means to prevent the corrosion caused by the dissolved O_2 and the weakly acidic solution. The optimum PAM concentration was 1 g L^{-1}. Too much PAM will reduce the ion conductivity of the electrolyte, and too little cannot form a perfect absorption layer [88]. In addition, the co-deposition of organic additives onto the electrode surface may causes a side reaction [89]. so the amount of additive should be controlled.

1.5.4 Introduction of a surfactant in the aqueous electrolyte:

The utilization of a surfactant in an aqueous electrolyte can solve the problems of the narrow electrochemical stability window and inhibit the evolution of hydrogen or oxygen. Sodium dodecyl sulfate (SDS) showed advantages for widening the electrochemical stability window of aqueous batteries (Fig. 7c), suppressing the dissolution of cathode materials and inhibiting the corrosion of zinc. In an electrolyte with SDS, the full battery exhibited about twice the capacity over the pristine electrolyte and a high capacity retention of 95% after 200 cycles [90].

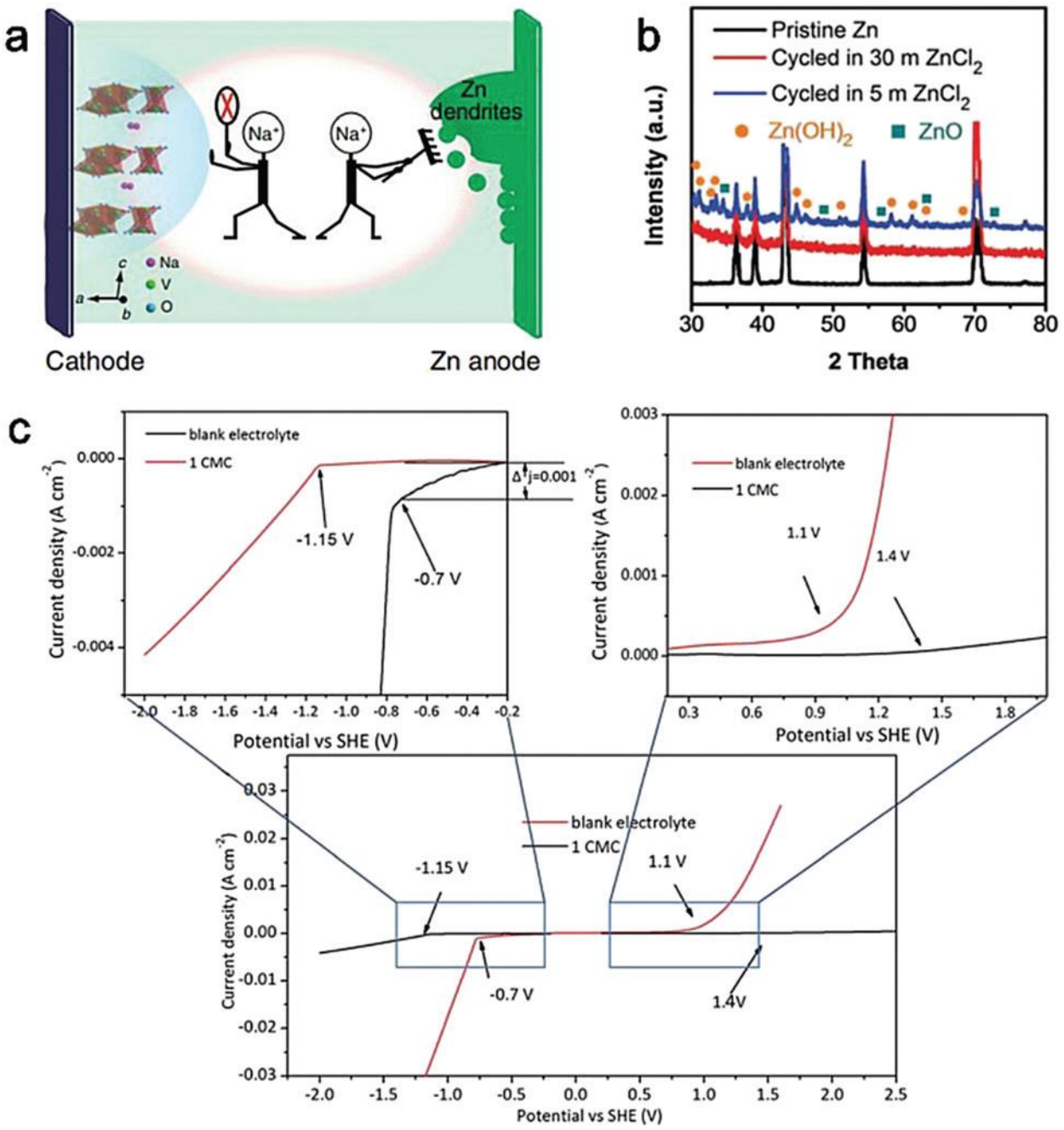

Figure 7. (a) Na_2SO_4 additive inhibited the dissolution of NaV_3O_8-1.5H_2O and the formation of Zn dendrites. (b) The ex situ XRD patterns of the pristine Zn metal and Zn electrodes cycled in 5 and 30 M $ZnCl_2$ electrolytes at 0.2 mA cm^2.(c) The electrochemical stability window of the electrolyte with and without sodium dodecyl sulfate (SDS) measured by linear sweep voltammetry on titanium grid electrodes versus Ag/AgCl at 10 mV s^{-1}

1.6 Electrochemical techniques:

Electrochemical methods are analytical techniques that use a measurement of potential, charge, or current to determine the concentration of an analyte or to characterize the chemical reactivity of an analyte. Electrochemical techniques are commonly used for analytical measurements, and there are a variety of electrochemical methods with varying utility for quantitative and qualitative analysis. Typically, these methods are divided into four main groups: Potentiometry, Voltammetry, Coulometry, and Conductometry [91]. Here we present only some commonly used electrochemical methods.

1.6.1 Cyclic voltammetry (CV)

Cyclic voltammetry is a very important and useful electrochemical method that can be used to study the redox behavior of electrode material and the coupled chemical reactions to determine the reaction mechanism, the stability of reaction products, the presence of intermediates in redox reactions, the kinetics of electron transfer, etc. [92]. In the CV experiment, the potential of the working electrode is increased linearly with time. Unlike linear voltammetry, once the set potential is reached, the potential of the working electrode is ramped in the opposite direction to return to the initial potential, as shown in Figure 8. These cycles of potential ramp can be repeated for many times
In the CV test, the potential is measured between the working electrode and the reference electrode, while the current is measured between the working electrode and the counter electrode. The current at the working electrode is plotted against the applied voltage to obtain the cyclic voltammogram curve, as shown in Figure 8. If we apply a reduction potential from V1 to V2, the cathodic current will increase over this period, assuming there is a reducible analyte in the system. At some point after the analyte reduction potential is reached, the cathodic current will decrease as the concentration of the reducible analyte is depleted. If the redox couple is reversible, the reduced analyte will be re-oxidized during the reverse scan (from V2 to V1), resulting in a current with reversed polarity (anodic current) as before. The more reversible the redox couple, the

more similar the oxidation peak is to the reduction peak. In a monoelectronic process, the oxidation and reduction peaks are about 60 mV apart. The ratio of the peak currents at the anode (I_{pa}) and cathode (I_{pc}) is 1 for a reversible system. The peak currents are proportional to the square root of the scan rate, as expressed in the Randles-Sevcik equation:

$$Ipa = 2.69 * 10^{C} z^{\frac{3}{2}} CAD^{\frac{1}{2}} v^{\frac{1}{2}}$$

Where I_{pa} is the anodic peak current, z is the number of electrons involved in the reaction, C is the bulk concentration, A is the electrode surface area, v is the scan rate, and D is the diffusion coefficient.

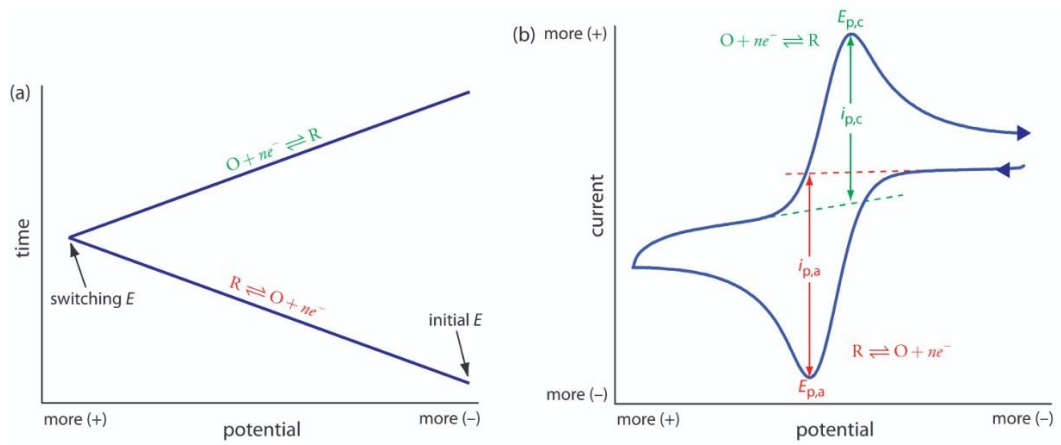

Figure 8. (a) One cycle of the triangular potential-excitation signal showing the initial potentialand switching potential; (b) The resulting cyclic voltammogram showing the measurement of the peak currents and peak potentials

1.6.2. Galvanostatic charge-discharge technique

Galvanostatic alludes to an explore procedure whereby an anode is kept up at a steady current is an pure electrolyte. This strategy is utilized to think about the execution of the battery over the lifetime of the cycling, erosion rate and electrochemical responses. In galvanostatic test, the altern is plotted in potential verses time at consistent current (figure 9). Amid the galvanostatic cycling of batteries, the charge and release current are regularly communicated as a C-rate, calculated from the battery ostensible capacity, i.e., the capacity esteem the battery has when totally charged. The C-rate may be a degree of the rate at which a battery is totally charged or released, relative to its ostensible capacity. For case, a C-rate of 1C implies that the current essential for total charge and release in one hour is connected. In battery investigate, it's common to utilize a C-rate of 0.1C, to charge and release a battery in ten hours. The current i(A) is calculated duplicating the C-rate by the proportion between the battery nominal C_{max} (Ah) and one hour time (h)

$$i(A) = c - rate * \frac{C_{max}(Ah)}{1(h)}$$

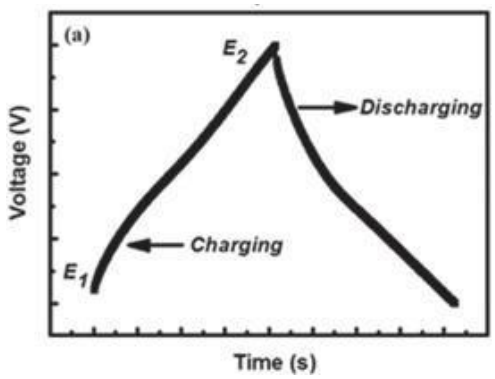

Figure 9. Galvanostatic charge-discharge curve

Normally for the galvanostatic cycling test, we will assemble some coin cells. The commonly used coin cell cases are 2032/2025. Both are 3 V button cell, around 20 mm in diameter, but the 2032 is 3.2 mm thick while the 2025 is 2.5 mm thick. Except the coin cell case, inside the coin cell are stacked layers, as show in figure 10. From the top to bottom, there are spacer (stainless steel Wave-spring/ space Disk), anode, separator, and cathode. After having been

stacked, coin cells are closed by means of a mechanical machine.

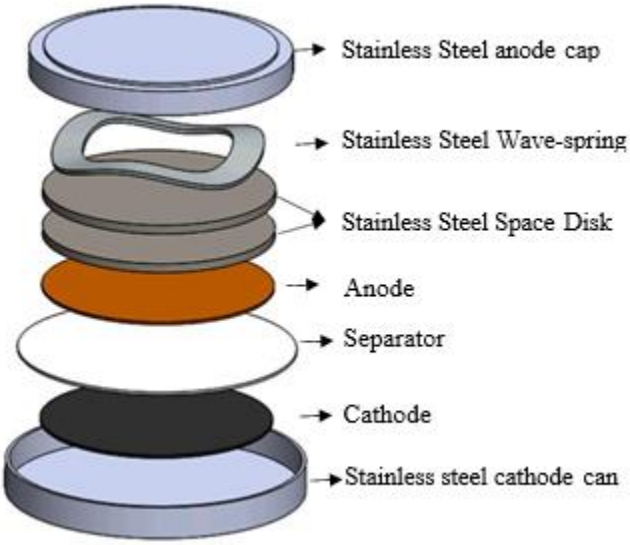

Figure 10. The schematic and assembling of coin cell.

2. Experimental part

2.1 Synthesis of Manganese Hexacyanoferrate (MnHCF) and its derivatives

MnHCF was synthesized using simple reproducible co-precipitation method [97]. The solutions of manganese sulfate monohydrate ($MnSO_4 \cdot H_2O$) and sodium ferrocyanide decahydrate($Na_4[Fe(CN)_6] \cdot 10H_2O$) (0.1 L, 0.1 M each) were prepared and added drop wise under the nitrogen flow to the solution of sodium sulfate Na_2SO_4 (0.1 L, 0.1 M) by means of a peristaltic pump at a rate of 4 mL min^{-1}. During the addition, the reaction batch was stirred at constant temperature (40 ± 2 °C) using a thermos stated bath and was stopped several minutes after the complete runover of the reagents. The obtained solution was aged for 5 days and the precipitate was collected via several consecutive centrifugation at 4000 rpm for 20 min using test tubes. After removing the supernatant, the precipitate was washed three times with distilled water, and then dried at 60 °C for 48 h.

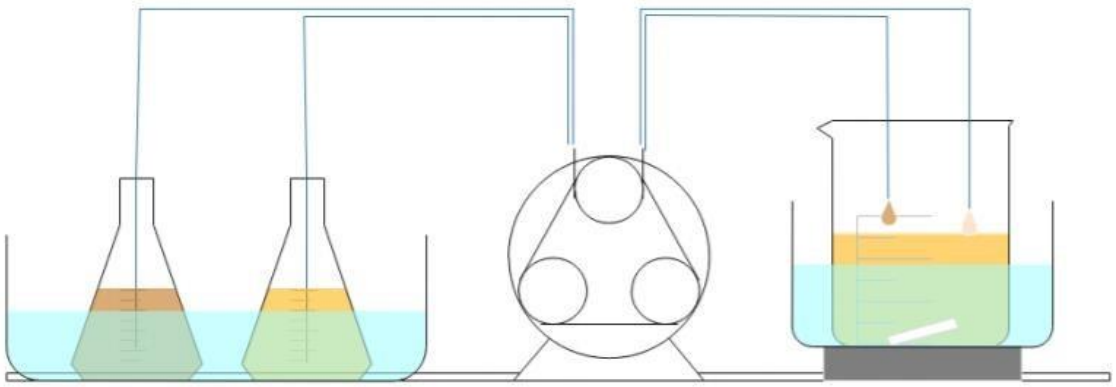

Figure 11. Experimental set-up adopted for the synthesis of Na-rich MnHCF [96]

The same procedure was used for synthesis of MnHCF derivatives (MnHCF-A with addition of ascorbic acid). The additional reagents (Ascorbic acid) were added on the first stage to the solution of $MnSO_4$ with the same concentration and pumped directly to the Na_2SO_4 solution under the same conditions as was mentioned previously

Table 2. Masses of reagents for synthesis of MnHCF and its derivatives

	M_w (g mol^{-1})	m (g)	c (M)
$MnSO_4 \cdot H_2O$	169.01	1.6901	0.1
$Na_4[Fe(CN)_6] \cdot 10H_2O$	484.06	4.8407	0.1
Na_2SO_4	142.04	1.4223	0.1
Citric acid	192,12	1.9201	0.1
Ascorbic acid	176.12	1.7617	0.1

2.2 electrode preparation:

To prepare the cathode slurry for Cyclic Voltammetry tests, 75 mg of synthesized compound and 20-25 mg of conducting agent (Super C65, IMERYS) were mixed properly in a mortar. After the addition of 5 mg of binder (PTFE, Solef 6020, Solvay polymer specialties), the obtained mixture was grinded around one hour until obtaining the homogenous thin solid slice. Then we used a puncher to get 8 mm (diameter) pellets with a mass density of around 5∼10 mg/cm2, then an aluminum mesh was used to fix the pellet. Full. Before the actual test the electrode is soaked in the corresponding electrolyte solution and left under vacuum for 2 hours.

2.3 Electrochemical tests

The electrochemical properties of the obtained material were evaluated in three-electrode mode: the active material as working electrode, zinc sheet as reference electrode and counter electrode. Full coin cells were assembled by using metal Zn sheet as anode and MnHCF pellet as cathode in different electrolytes.

Cyclic voltammetry (CV) was performed by means of CHInstru- ments Model 660. The CV test was conducted in potential range 1∼1.9 V vs Zn^{2+}/Zn in 3 M $ZnSO_4$ aqueous solution.

Galvanostatic cycling with potential limit (GCPL) was conducted in 1< E <1.9 V vs Zn^{2+}/Zn potential window at different current densities. Cycling started after a rest time (3 h) at OCP condition with a positive imposed current.

2.3.1 El cell technique:

There were 2 ports with the name A and B, in port A working electerode was connected and from port B the electrolyte was injected inside. As it is shown in Fig 12, to assemble the El-cell, first we put the anode which was a small sheet of Zn ion, then we put separator and then the pellets of cathode with bigger diameter of coin cell pellets, to have higher connection between cathode and anode, then the Al foil and at last we put a window made of glass or Al. then by using a syringe the electrolyte was injected inside the cell. the working electrode (red cable) and counter electrode (blue cable) was connected as it is shown in Fig 12.

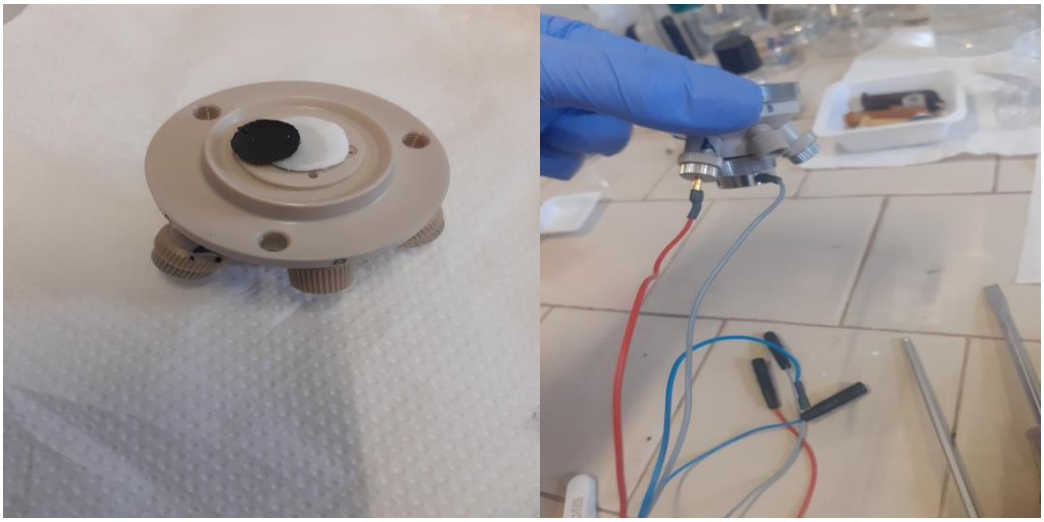

Figure 12. The schematic and assembling of El cell

2.4 Characterization

Microwave plasma-atomic emission spectrometer (MP-AES) composition analysis was done by means of MP-AES 4210 atomic emission spectrometer. During the test, first different concentration (0,10ppm, 20 ppm, 30 ppm and 40 ppm) standard solution of Fe, Mn and Na was prepared (diluted by 0.5M nitric acid); then the sample was solved in 0.5M nitric acid. Three different analytical lines (wavelengths) were chosen for each element during the test.

3. Results and discussion

Increasing the Na content in cathode materials is one of the effective ways to achieve higher energy density. In our case, we tried to obtain sodium iron hexacyanoferrate with higher sodium content by controlling the reducing agent and reaction atmosphere during synthesis. For that purpuse ascorbic acid was added on the first stage to chelate the Mn^{2+} in order to slow down the nucleation of NaMnHCF and promote homogeneous and near-stoichiometric crystal growth. You et al. reported that sodium iron hexacyanoferrate with high Na content ($Na_{1.63}Fe_{1.89}(CN)_6$) can be obtained with addition of ascorbic acid[99], whereas Tang and coworkers proposed the following mechanisms for citrate-assisted crystallization process of the $Na_{1.90}Mn[Fe(CN)_6]_{0.93}$: the Mn^{2+} ions were first coordinated with citrate ions to form Mn^{2+}·citrate3− chelate and then slowly coprecipitated with $Fe(CN)_6^{4-}$ to form the target products (as shown in Figure 13) [100].

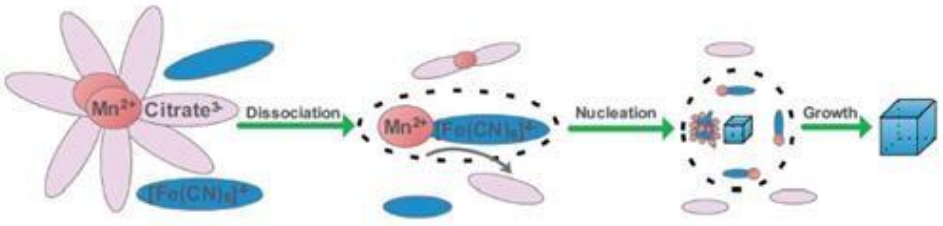

Figure 13. Schematic representation of the citrate-assisted controlled crystallization process for thesynthesis of $Na_xMnFe(CN)_6$ samples

The stoichiometry of resulting sodium rich manganese hexacyanoferrate and its derivatives are calculated based on MP-AES composition analysis and summarized in Table 3. As we can see, in defective manganese hexacyanoferrate compounds the content of sodium is gradually increased from 1.98 in MnHCF to 2.17 in MnHCF-A that is in agreement with literature resources.

Table 3: Calculated formula of MnHCF and its derivatives

MnHCF	$Na_{1.98}Mn\ [Fe(CN)_6]_{0.7}$
MnHCF-A	$Na_{2.17}Mn\ [Fe(CN)_6]_{0.72}$

According to the literature, NaMnHCF has three different structures when precipitated under different conditions. Generally, room-temperature precipitation leads to a cubic phase with low interstitial Na^+($x > 1.5$) and high water content (>12 wt%), whereas precipitating at elevated temperature can increase the Na^+ filling ($1.5 < x < 1.8$) and reduce the interstitial water and Fe $(CN)_6^{4-}$ vacancies, resulting in a monoclinic structure that is slightly distorted ($\beta = 92.1^o$) from cubic. However, the remaining water in monoclinic NaMHCF is still too high (>10 wt%), which is unfavorable for the cycling stability of NIBs. Rhombohedral NaMHCF is the only phase that containsan acceptable level of water (<5 wt%), but the synthesis usually requires a long dehydration process in high vacuum or/and at high temperature. In our case, we performed the synthesis at 40ºC under nitrogen atmosphere and expect to have monoclinic structure. We calculate theoretical diffraction pattern based on the structural parameters reported in the article [65] and profile parameters derived from silicon sample.

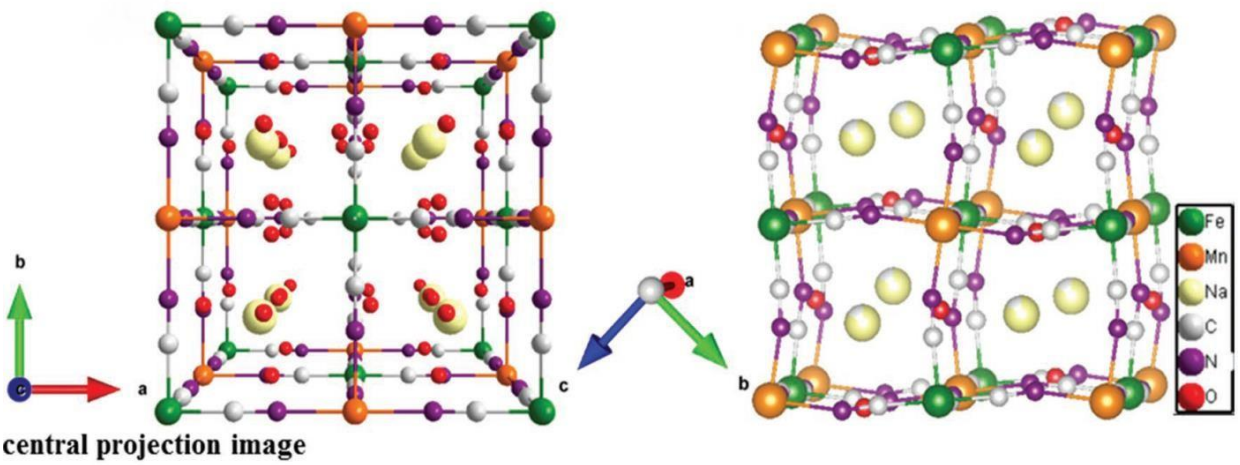

Figure 14. Schematic model of cubic and monoclinic Na-rich MnHCF compound

3.1 Electrochemical application:

Electrochemical measurement of synthesized samples was performed by the means of cyclic voltammetry. For that purpose, series of pellets were tested in 3M $ZnSO_4$,3M $ZnSO_4$ +1M $MnSO_4$,3M Zn $(OTF)_2$, in coin cell.

3.1.1 Aqueous electrolyte system:

In general, the requirements for an ideal electrolyte are as follows: (1) wide potential window;(2) high ionic conductivity; (3) high chemical and electrochemical stability; (4) high chemical and electrochemical inertness to ES components (e.g., electrode, current collectors and packaging); (5) wide operating temperature range; (6) well-matched with the electrolyte material; (7) low volatility and flammability; (8) environmentally friendly; and (9) low cost. Actually, it is very difficult for an electrolyte to meet all these requirements, and each electrolyte has its own advantages and shortcomings.

The Electrochemistry performance of the as-prepared sample was investigated in aqueous electrolyte Compared to organic system electrolyte, the aqueous system batteries show several benefits: (i) Safety. Aqueous system batteries avoid the using of volatile, flammable and toxic organic electrolytes, avoid the potential safety issue and environment concern; (ii) Easy to prepare. Aqueous system batteries don’t need rigorous manufacturing conditions, and the price of electrolyte solvent and salt also cheap; (iii) high ion conductivity. The ion conductivity of the aqueous electrolyte is higher than those of

organic electrolyte by 2 orders of magnitude. So, TiHCF electrode material was first tested in aqueous electrolyte [66].

According to the literature, two pair of oxidation/reduction peaks should be observed in MnHCF material: first one is attributed to the redox transitions of the carbon-coordinated Fe^{2+}/Fe^{3+} couple, whereas second – to the nitrogen-coordinated $Mn^{2+/}Mn^{3+}$ couple in the PB framework. For example, Cui and coworkers reported that three electrochemical processes have been clearly visible at 0.8, 0.9, and 1.4 V (vs. SHE) in manganese hexacyanoferrate sample. The electrochemical processes at 0.8 and 0.9 V are mainly attributed to the electrochemical activity of Fe (Mn^{II}–N-C–$Fe^{III/II}$), and they correspond to the extraction/insertion of sodium ions from the rhombohedral and cubic phases, respectively. Mn is primarily responsible for the poorly reversible electrochemical process at 1.4 V ($Mn^{II/III}$–N-C–Fe^{III}). This irreversibility can be explained by the combined effects of internal charge-transfer processes, hybridization between the Mn and N orbitals, and the oxidation of the aqueous electrolyte at this elevated potential.

3.2 analysis of MnHCF and MnHCF+AC -3M $ZnSO_4$ by coin cell and El cell technique:

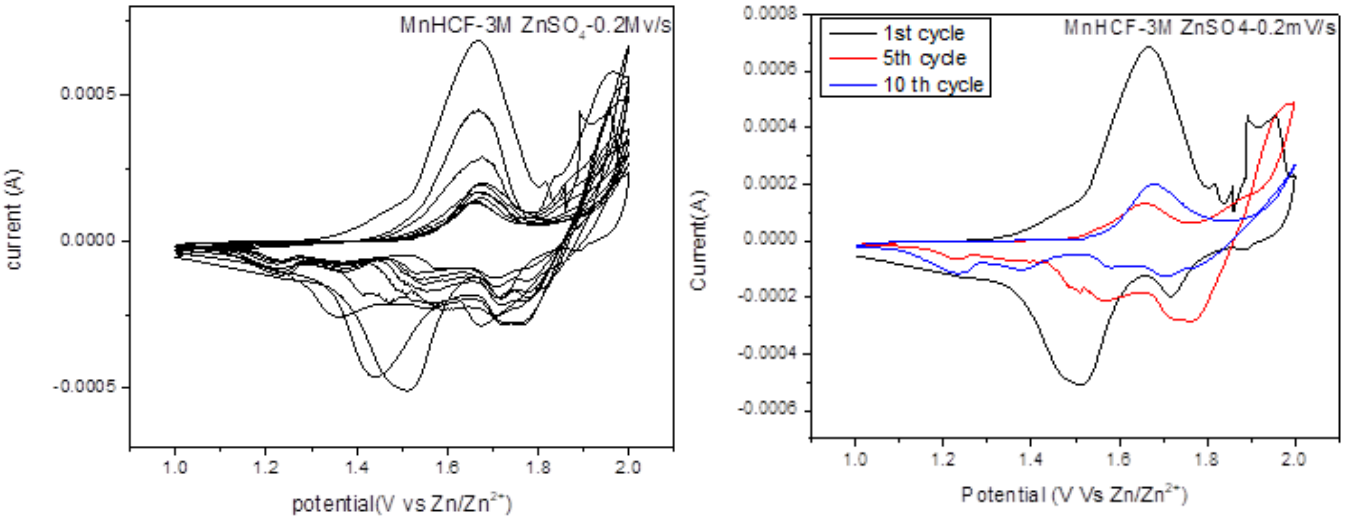

Figure 15. a) Cyclic voltammetry of coin cell MnHCF in 3M $ZnSO_4$ electrolyte at 0.2 mV/S scan rate b)zoom-in CV curve of MnHCF.

As shown in figure 15 in 3M $ZnSO_4$ electrolyte, Cyclic voltammetry (CV) curves were recorded at 0.2 mV/s scan rates in the voltage range from 1 to 2 V (vs Zn^{2+}/Zn). only one anode peak appeared at around 1.63 V, but two new cathode peaks were observed at 1.26 and 1.39 V. At least a couple peak in both oxidation and reduction is observed. As shown in 15 (a, b), the CV profile in the first cycle is slightly different from the following ones. The oxidation peak at 1.94 V can be related to the extraction of Na^+ from electrode during the first charge process , while the two reduction peaks at 1.74 V and 1.54 V during the first discharge process can be attributed to the insertion of Zn^{2+} and Na^+ , respectively. Two oxidation peaks at 1.68 V and 1.89 V were observed in the successive cycles, which might correspond to Zn-extraction from MnHCF cathode as the Fe^{II} and Mn^{II} states undergo oxidation to the Fe^{III} and Mn^{III} states. Furthermore, except for the reduction peak at 1.77 V, two new reduction peaks at 1.40 and 1.25 V appeared, and in light of the literature reports [21,39], they can be attributed

to the reduction of Fe^{3+} to Fe^{2+}. The current intensity of these two peaks was increasing cycle by cycle, as well as the oxidation peak at 1.68 V. This behavior was maybe related to the gradual activation of the electrode and/or the structural transition with insertion/extraction of Zn-ions.

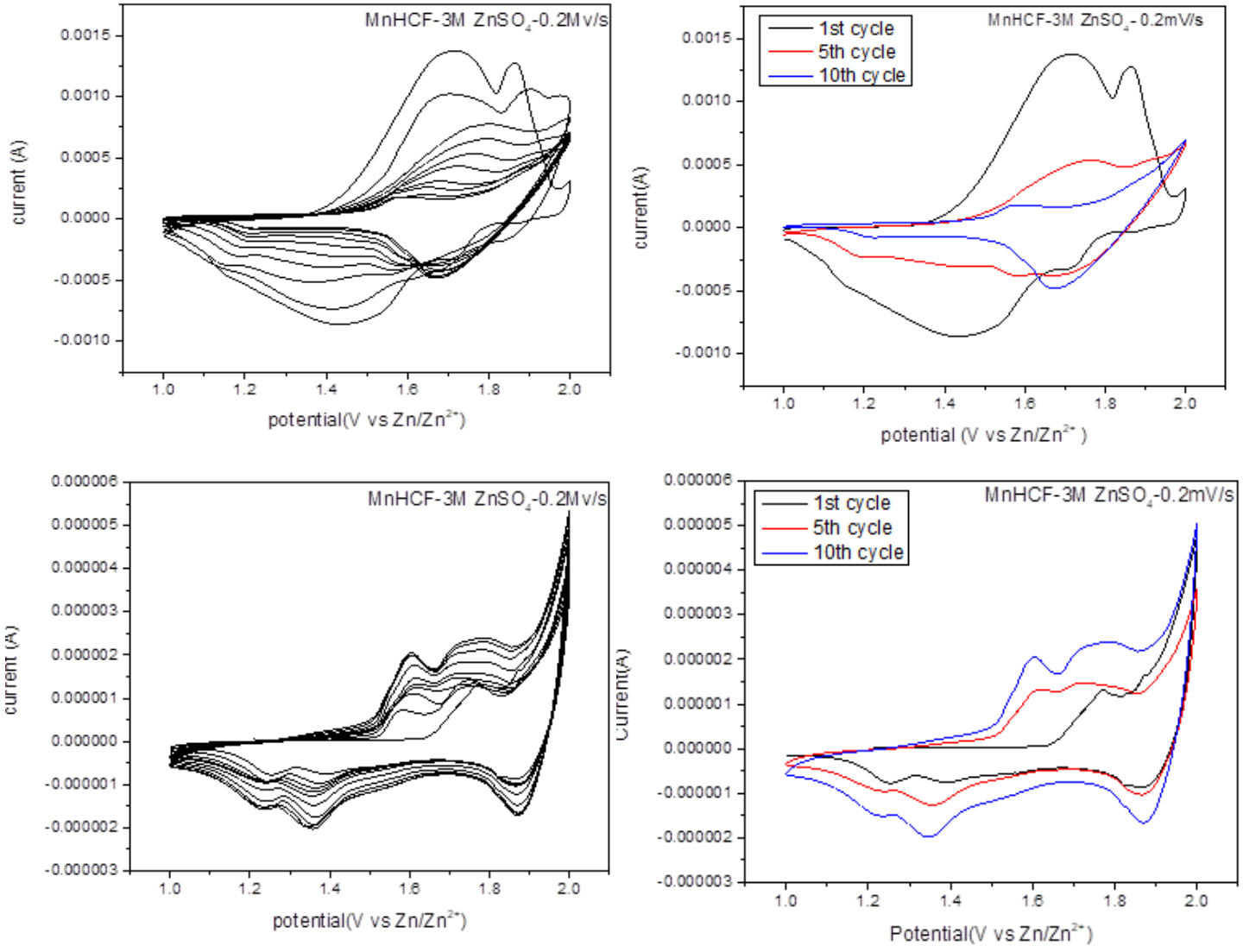

Figure 16. Cyclic voltammetry of MnHCF- 3M $ZnSO_4$ El cell sample

As shown in figure 16 in 3M $ZnSO_4$ electrolyte, Cyclic voltammetry (CV) curves were recorded at 0.2 mV/s scan rates for two identically prepared same samples to see if the results are the same or not, in the voltage range from 1 to 2 V. 2. The CV profile in the first cycle is slightly different from the following ones. For the first cycle in the first sample there are 2 oxidation peaks at around 1.71 V and 1.81 V and two reduction peaks at around 1.66 V and 1.45 V while in the 5th cycle there is only 1 oxidation peak at around 1.72 V and reduction at 1.62 V and in the 10th cycle the oxidation peak at around 1.57 V and reduction at 1.68 V. for the second sample for the first cycle there

are 2 oxidation peaks at around 1.67 V and 2 V and two reduction peaks at around 1.24 V and 1.87 V while in the 5th cycle the oxidation peaks are at around 1.61 Vand 2 V and reductions at 1.36 V and 1.86 V and in the 10th cycle the oxidation peak at around 1.6 V and 2 V and reductions at 1.35 V and 1.88 V.

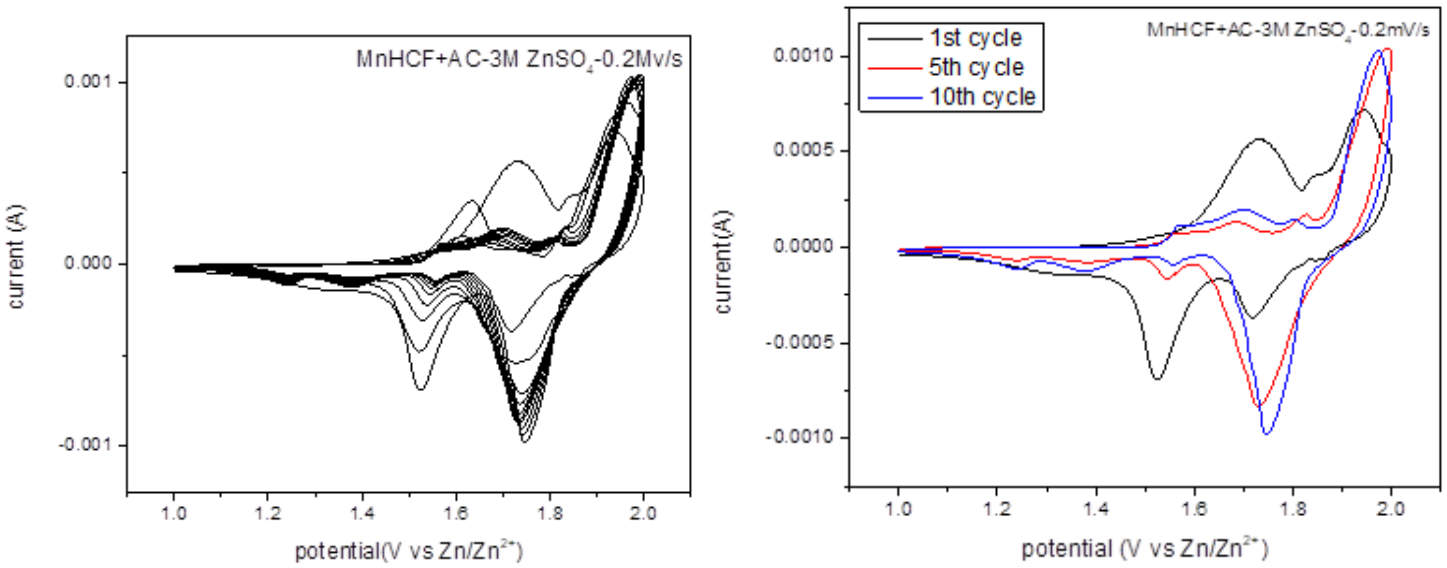

Figure 17. Cyclic voltammetry of MnHCF+AC- 3M $ZnSO_4$ coin cell sample

Turning to MnHCF+AC sample, cycling voltammetry tests were run in the 1 < E <2V . SCE potential window at 0.2 mV/s scan rates. In Figure 17 in the first cycle we see two couples of oxy-reduction peaks are observed. we can see the reduction peak centered around 1.52 V and 1.72V and oxidation peaks centered at 1.73 V and 1.94 V which again can be attributed to Fe^{2+}/Fe^{3+} redox couple, while for the 5th cycle the oxidation peak is around 2.0 V and reduction around 1.73 and also for the 10th cycle the oxidation around 1.92 V and reduction around 1.75 V.

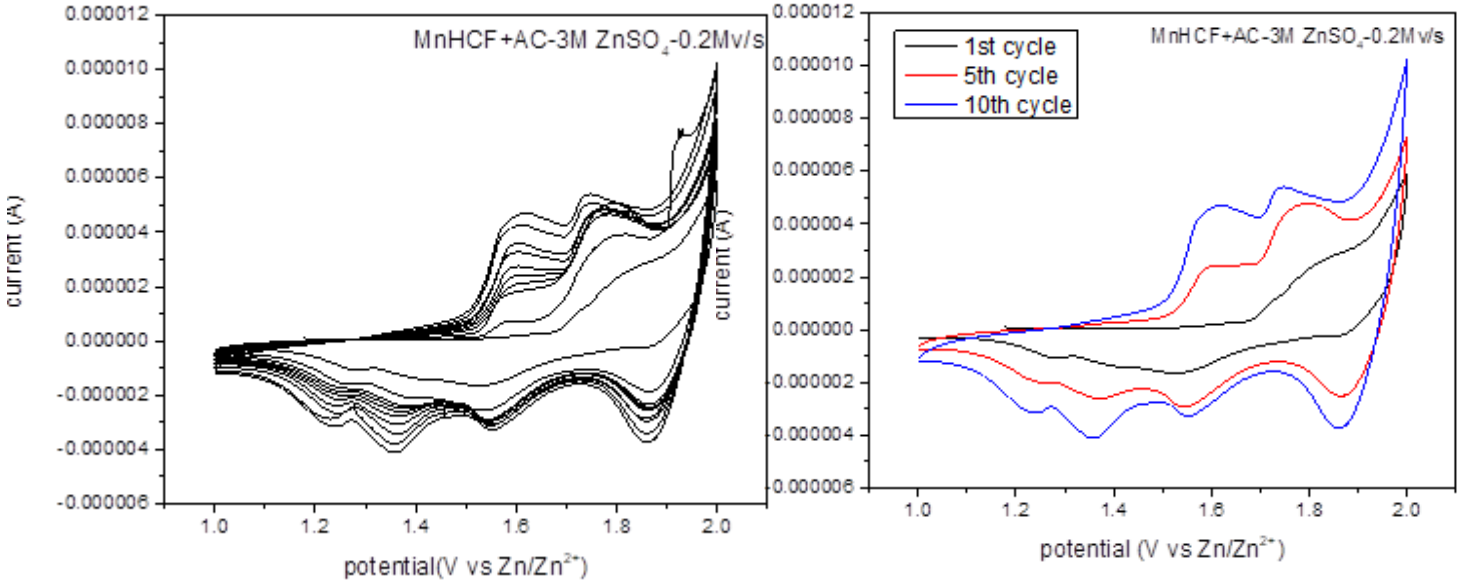

Figure 18. Cyclic voltammetry of MnHCF+AC- 3M $ZnSO_4$ El cell sample

By Turning to MnHCF+AC sample for the El-cell samples as it is shown in Figure 18 in the 5th and 10th cycle there are 2 oxidation -reduction peaks while in the first cycle there is only 1 oxidation – reduction peak.

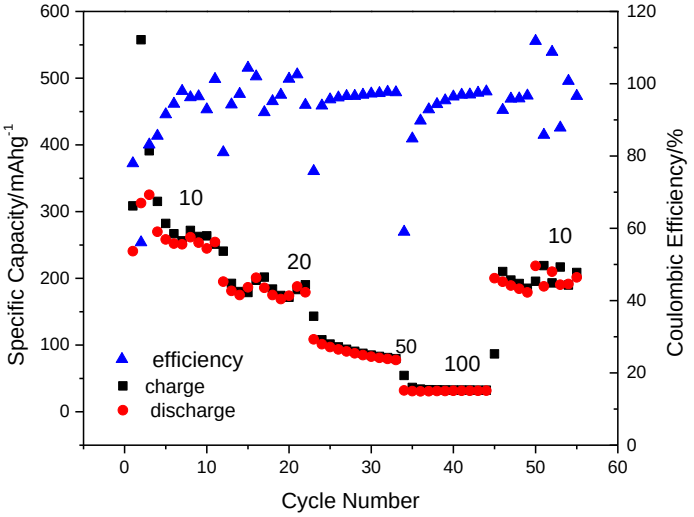

Figure 19. Rate capability of MnHCF-3M $ZnSO_4$ with different (10,20,50,100 mAg^{-1}) current densities

The rate capability on MnHCF in $ZnSO_4$ is depicted in Fig.19, in $ZnSO_4$ as the current density increases from 10 to 20,50 and 100 mAg^{-1} , the Zn/MnHCF battery delivers max discharge capacities of 200, 110 and 40 mAg^{-1} , respectively, when the current density decreases back to 10 mAg^{-1} , it can be restored to a high capacity of 210 mAg^{-1}, indicating good reversibility.

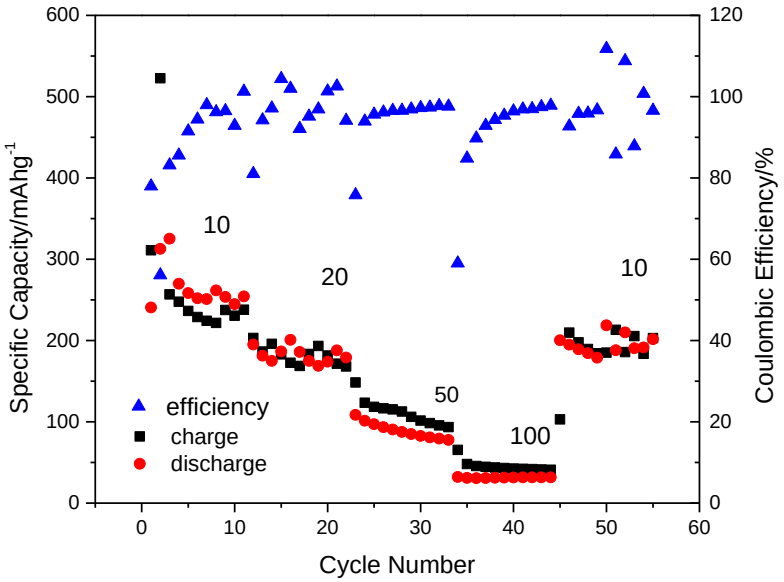

Figure 20. Rate capability of MnHCF+AC-3M $ZnSO_4$ with different(10,20,50,100 mAg^{-1}) current densities

The rate capability on MnHCF+AC in $ZnSO_4$ is shown in Fig.20, in $ZnSO_4$ as the current density increases from 10 to 20,50 and 100 mAg^{-1}, the Zn/MnHCF+AC battery delivers max discharge capacities of 200, 120 and 50 mAg^{-1}, respectively, when the current density decreases back to 10 mAg^{-1}, it can be restored to a high capacity of 210 mAg^{-1}, indicating good reversibility.

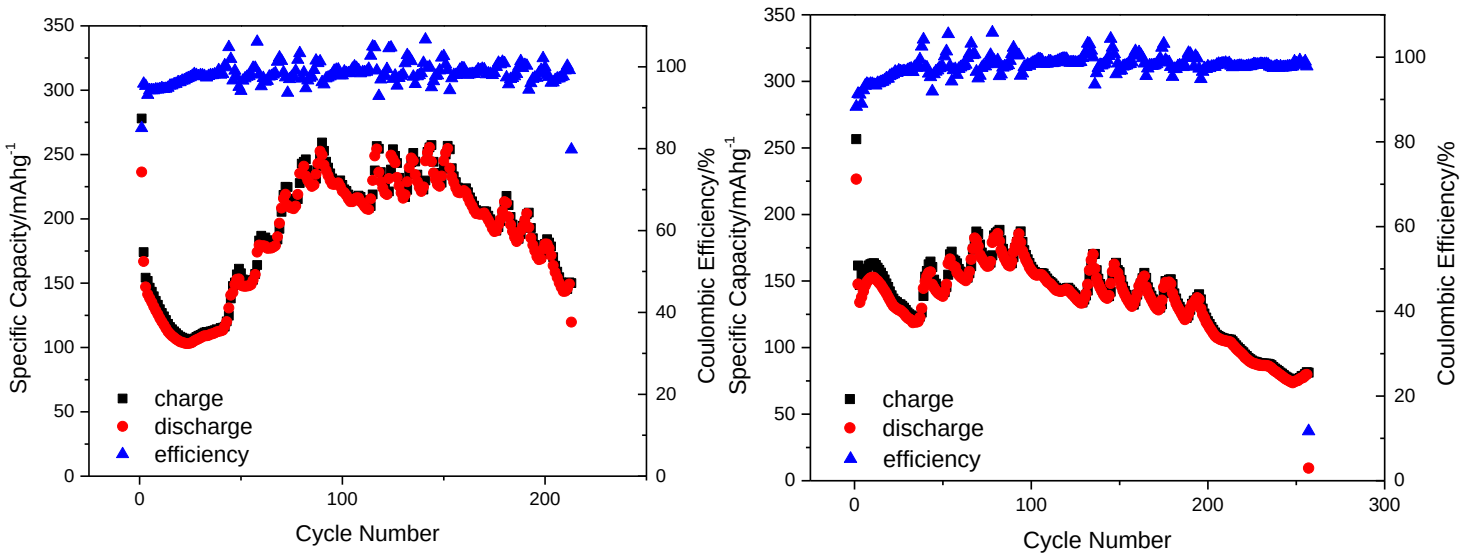

Figure 21. (a)long- term stability test of MnHCF-$ZnSO_4$ after 250cycle, (b) long term stability test of MnHCF+AC-3M $ZnSO_4$ after 250 cycle

The long- term stability is investigated for 2 different samples at a current density of 50mAg^{-1}. In Fig 21 (a) the initial discharge capacity of MnHCF is 150 mAhg^{-1}. The capacity increases to 250 mAhg^{-1} in the following 90 cycles, and then decreases in the subsequent 160 cycles. After 250 cycles, the discharge capacity is 140, which is 93% of the initial capacity, and 56% of the max capacity. In the second sample Fig 21(b) The initial discharge capacity of MnHCF-AC is 135 mAhg^{-1}. the capacity increases to 190 mAhg^{-1} in the following 100 cycles, and then decreases in the subsequent 150 cycles. After 250 cycles, the discharge capacity is 80, which is 60% of the initial capacity, and 42% of the max capacity.

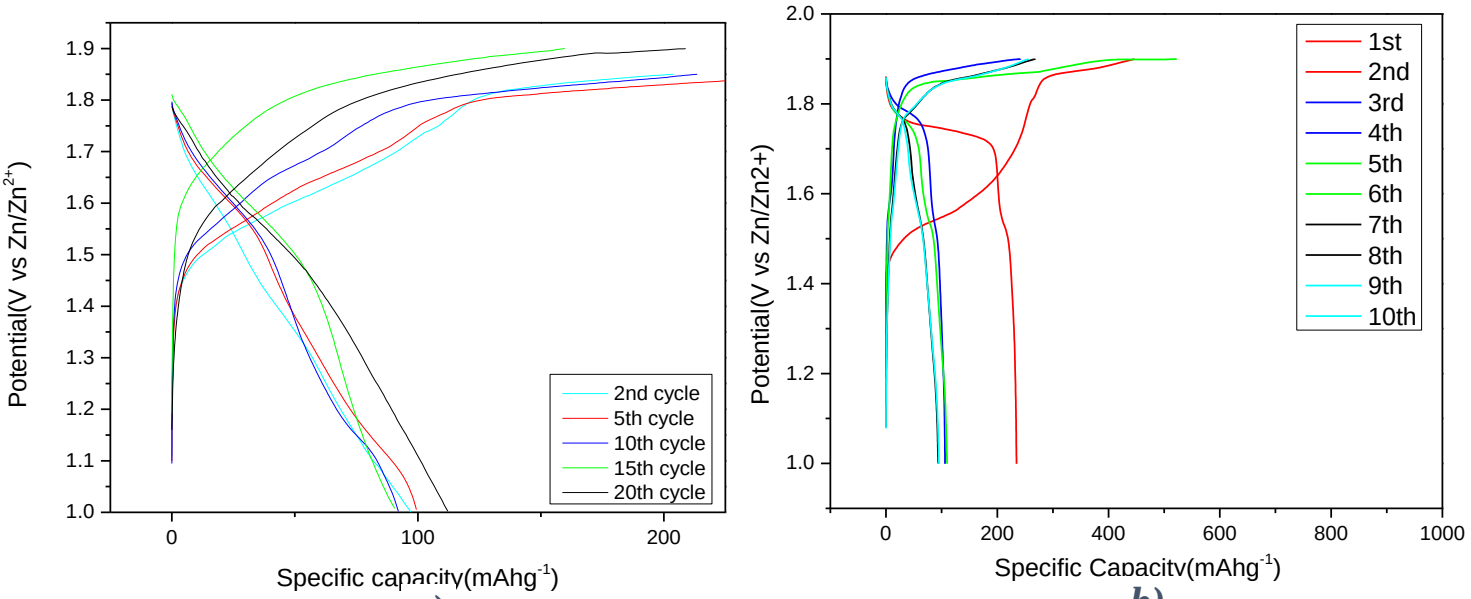

Figure 22. Galvanostatic charge/discharge curves (a)MnHCF and (b) MnHCF+AC-3M $ZnSO_4$ El cell

the Galvanostatic charge/discharge curves of MnHCF (Fig 22(a)shows a slope (1.2–1.6 V) and a long flat line (1.90 V) contribute a high charge capacity of 160 mA h g^{-1} for the first charge process at 50 mA g^{-1}, corresponding to the extraction of Mn^{2+} ions from the host structure. During this charge process, the Mn ions are removed from the host structure. In Fig22(b) for the second cycle there is a slope between 1.4 to 1.85 and a flat line around 1.85.

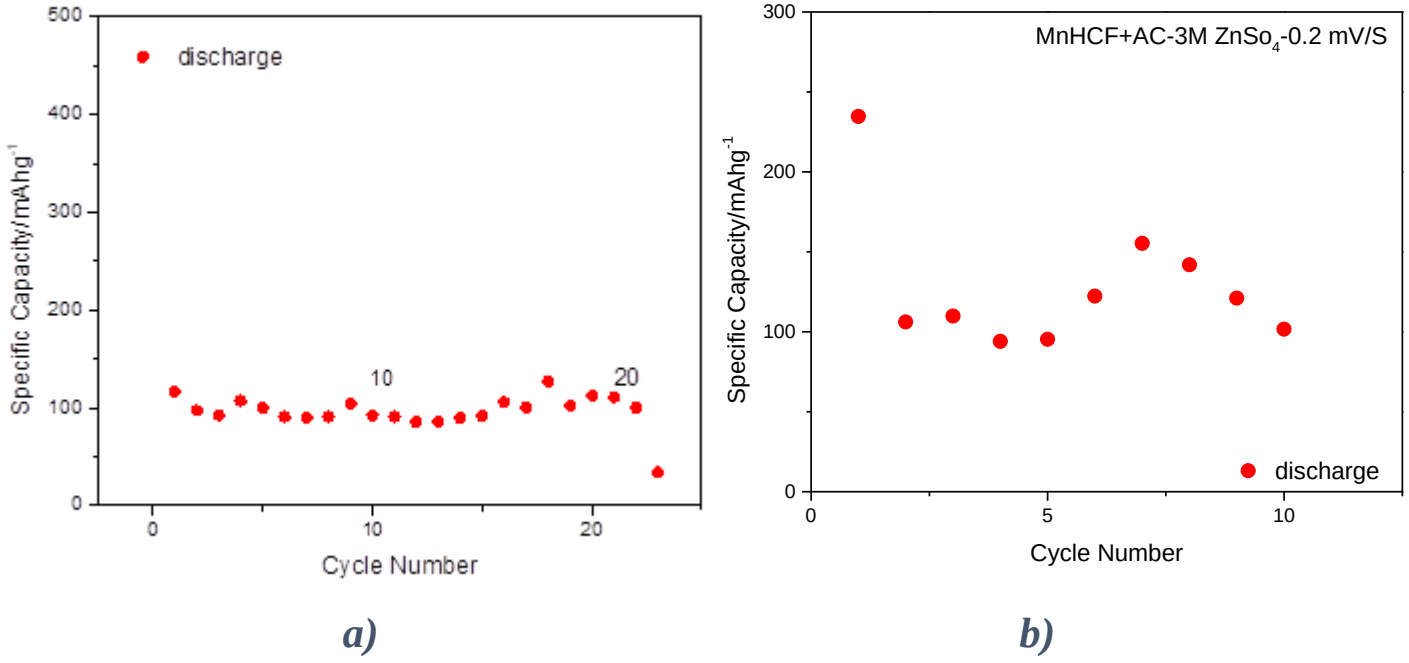

Figure 23. (a)long- term Stability test of MnHCF-$ZnSO_4$ after 250cycle, (b) long term Stability test of MnHCF+AC-3M $ZnSO_4$ after 250 cycle

The long- term stability is investigated for MnHCF and MnHCF+AC samples at a current density of 50 mAg^{-1}. In Fig 23 (a)The initial discharge capacity of MnHCF is 110 $mAhg^{-1}$ and the capacity stays almost the same in the following20 cycles, before the battery dies. In the second sample Fig 23(b) The initial discharge capacity of MnHCF is 110 $mAhg^{-1}$. the capacity decreases to 100 mAhg-1 in the following 4 cycles, and then increases in the subsequent 3 cycles. After 10 cycles, before the death of the battery the discharge capacity is 80 again reaches to 100.

3.3 CV and battery analysis of MnHCF and MnHCF+AC -3M $ZnSO_4$ +(0.1,0.5,1) M $MnSO_4$

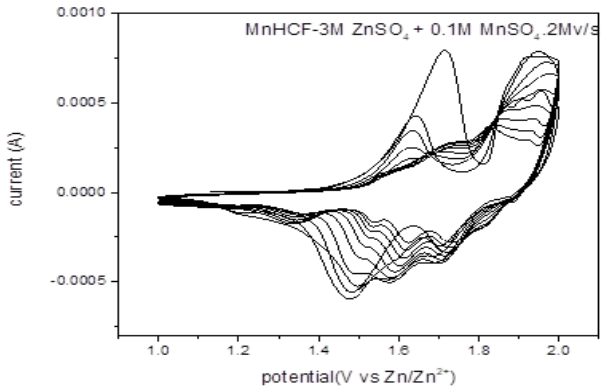

a)

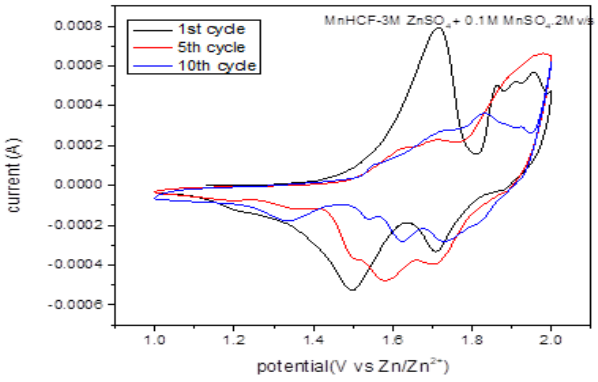

b)

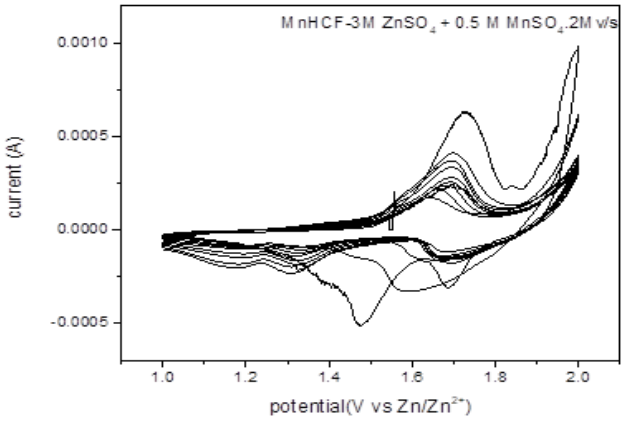

c)

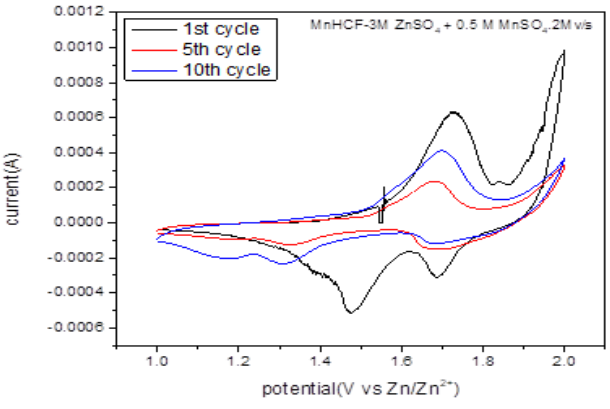

d)

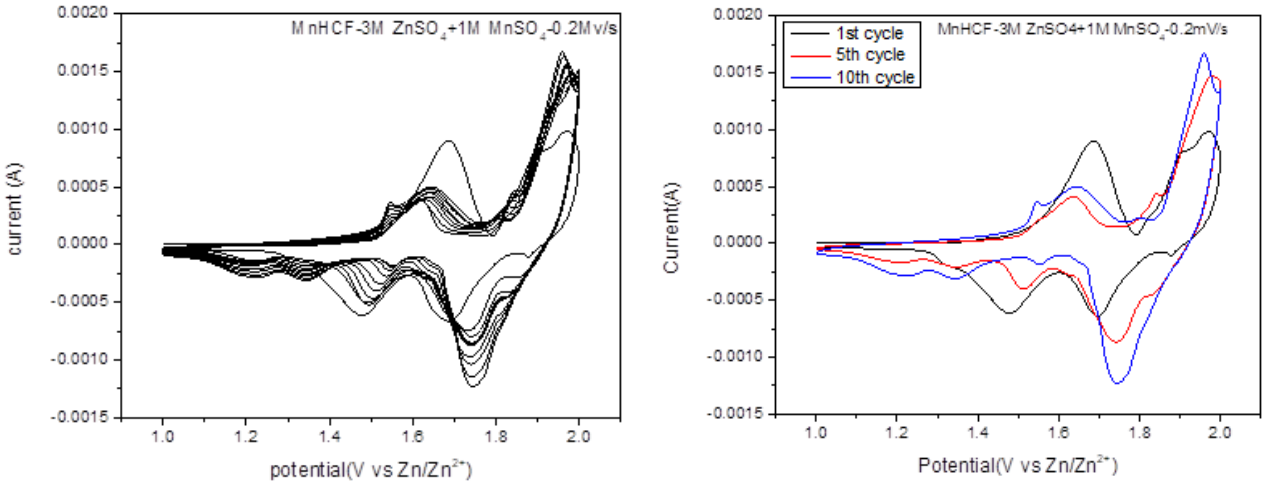

e) *f)*

Figure 24. Cyclic voltammetry of MnHCF -3M $ZnSO_4$ + (a)0.1, (b)0.5, (c)1 M $MnSO_4$ electrolyte

As shown in figure 24(a) by adding 0.1 M $MnSO_4$ salts to the previous electrolyte, Cyclic voltammetry (CV) curves were recorded at 0.2 mV/s scan rates in the voltage range from 1 to 2 V. In Fig 24(a, b) for the first cycle the CV profile in the first cycle is slightly different from the following ones there are two oxidation- reduction, cathode peaks at around 1.72 V and 1.96 V and anode peaks at around 1.49 V and 1.70 V. As shown in 24 (c, d), for all cycles there are 2 pair of oxidation-reduction peaks, in the first cycle, The oxidation peak at 1.94 V can be related to the extraction of Na^+ from electrode during the first charge process, while the two reduction peaks at 1.74 V and 1.54 V during the first discharge process can be attributed to the insertion of Zn^{2+} and Na^+, respectively. Two oxidation peaks at 1.68 V and 1.89 V were observed in the successive cycles, which might correspond to Zn-extraction from MnHCF cathode as the Fe^{II} and Mn^{II} states undergo oxidation to the Fe^{III} and Mn^{III} states, they can be attributed to the reduction of Fe^{3+} to Fe^{2+}. The current intensity of these two peaks was increasing cycle by cycle. This behavior was maybe related to the gradual activation of the electrode and/or the structural transition with insertion/extraction of Zn-ions. As shown in Fig 21(e, f), except the first cycle for all the following cycles, the oxidation and reduction occur at the same place which the oxidation happen at around 1.64 V and

1.99 V and reduction happen at around 1.5 V and 1.75 V.

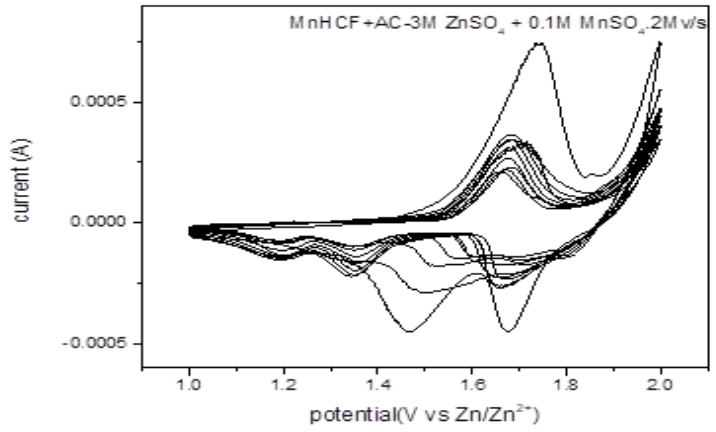

a)

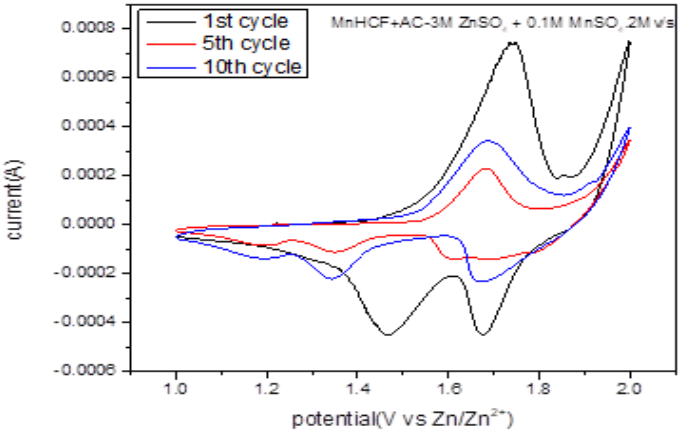

b)

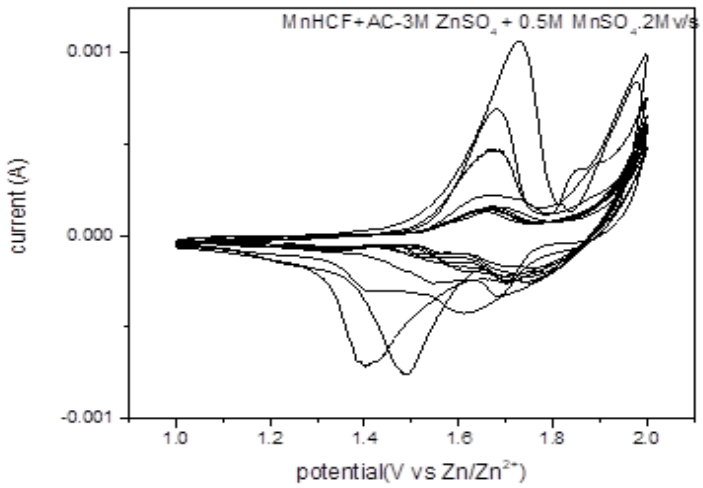

c)

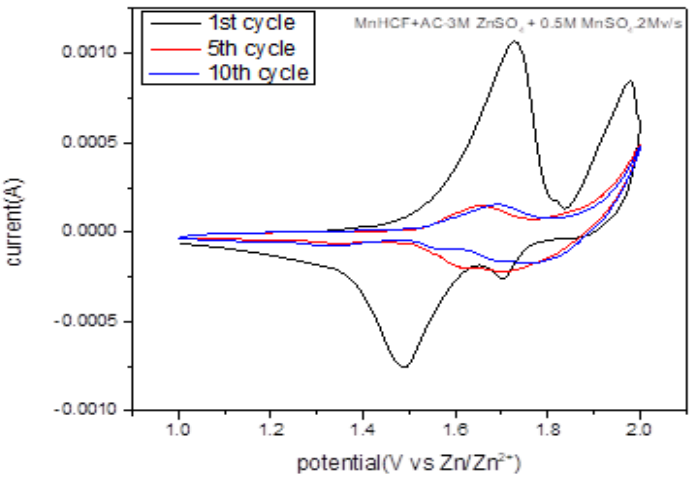

d)

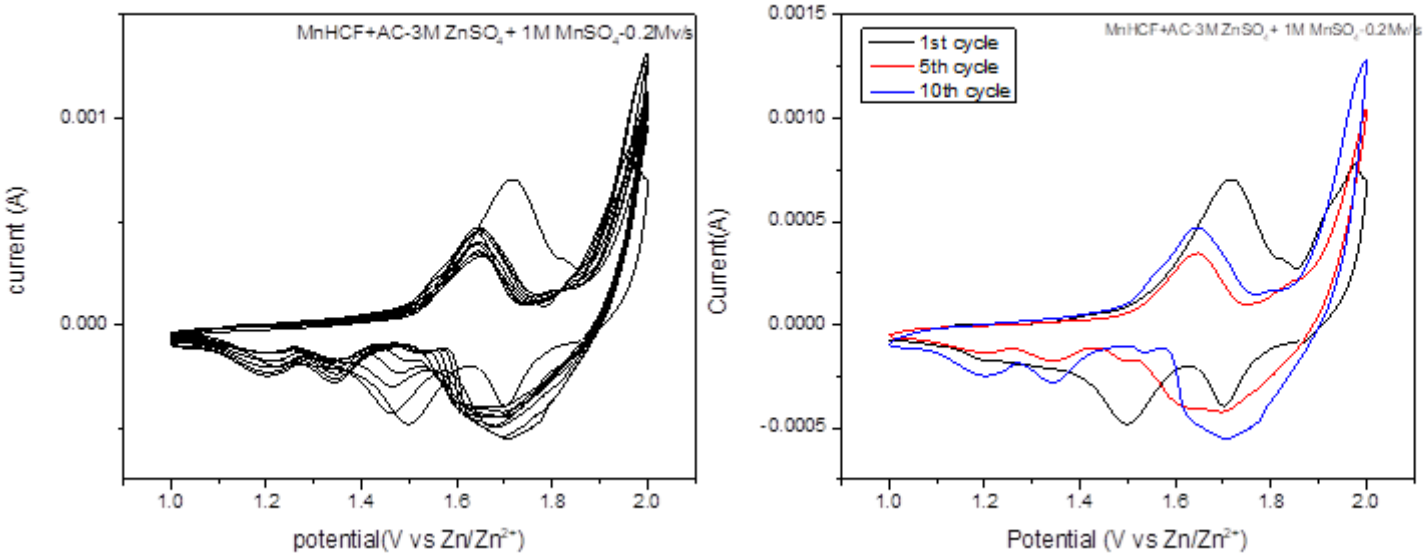

e) *f)*

Figure 25. Cyclic voltammetry of MnHCF+AC -3M $ZnSO_4$ + (a)0.1,(b)0.5,(c)1 M $MnSO_4$ electrolyte

As shown in Fig 25(a) by adding 0.1 M $MnSO_4$ salts to the previous electrolyte, Cyclic voltammetry (CV) curves were recorded at 0.2 mV/s scan rates in the voltage range from 1 to 2 V. in Fig 25(a, b) for the first cycle the CV profile in the first cycle is slightly different from the following ones there are two oxidation- reduction, cathode peaks at around 1.73 V and 1.99 V and anode peaks at around 1.46 V and 1.67 V. As shown in 25 (c,d),for all cycles there are 2 pair of oxidation-reduction peaks , in the first cycle ,The oxidation peak at 1.94 V can be related to the extraction of Na^+ from electrode during the first charge process ,while the two reduction peaks at 1.70 V and 1.49 V during the first discharge process can be attributed to the insertion of Zn^{2+} and Na^+, respectively. Two oxidation peaks at 1.68 V and 1.99 V were observed in the successive cycles, which might correspond to Zn-extraction from MnHCF cathode as the Fe^{II} and Mn^{II} states undergo oxidation to the Fe^{III} and Mn^{III} states, they can be attributed to the reduction of Fe^{3+} to Fe^{2+}. The current intensity of these two peaks was increasing cycle by cycle. This behavior was maybe related to the gradual activation of the electrode and/or the structural transition with insertion/extraction of Zn-ions. As shown in Fig

21(e,f), except the first cycle for all the following cycles, the oxidation peaks occur at the same place which the oxidation happen at around 1.63 V and 1.99 V.

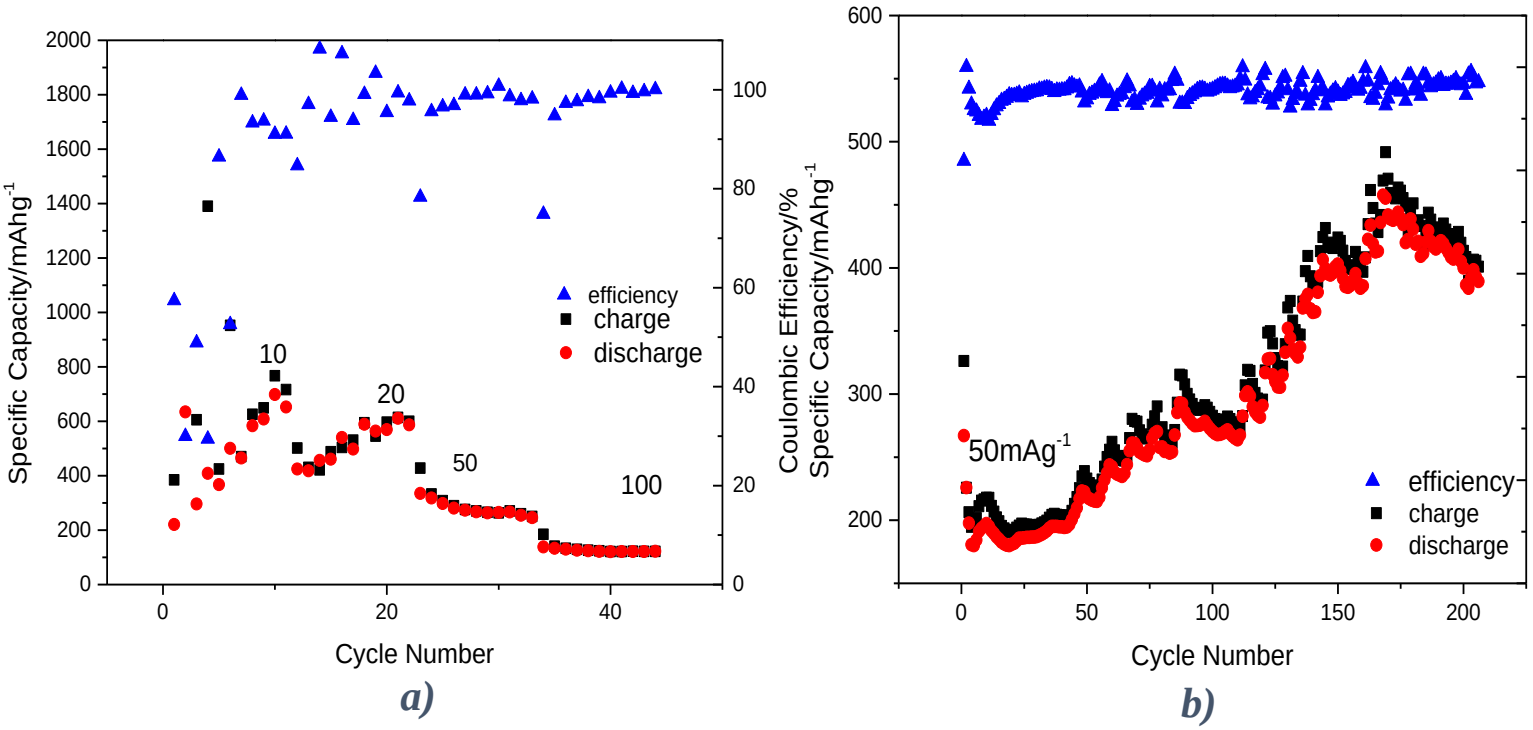

Figure 26(a)Rate capability of MnHCF-3M $ZnSO_4$+1M $MnSO_4$ with different (10,20,50,100 mAg^{-1}) current densities. (b) (a)long- term Stability test of MnHCF-$ZnSO_4$+1M $MnSO_4$

The rate capability on MnHCF in $ZnSO_4$+1M $MnSO_4$ is shown in Fig.26(a), as the current density increases from 10 to 20,50 and 100 mAg^{-1}, the Zn/MnHCF battery delivers max discharge capacities of 597, 315 and 125 mAg^{-1}, respectively, when the current density decreases back to 10 mAg^{-1}, it can be restored to a high capacity of 210 mAg^{-1}, indicating good reversibility.

The long- term stability is investigated at a current density of 50 mAg^{-1}. In Fig 26(b)The initial discharge capacity of MnHCF is 140 $mAhg^{-1}$. the capacity increases to 450 $mAhg^{-1}$ in the following 170 cycles, and then decreases in the subsequent 30 cycles.

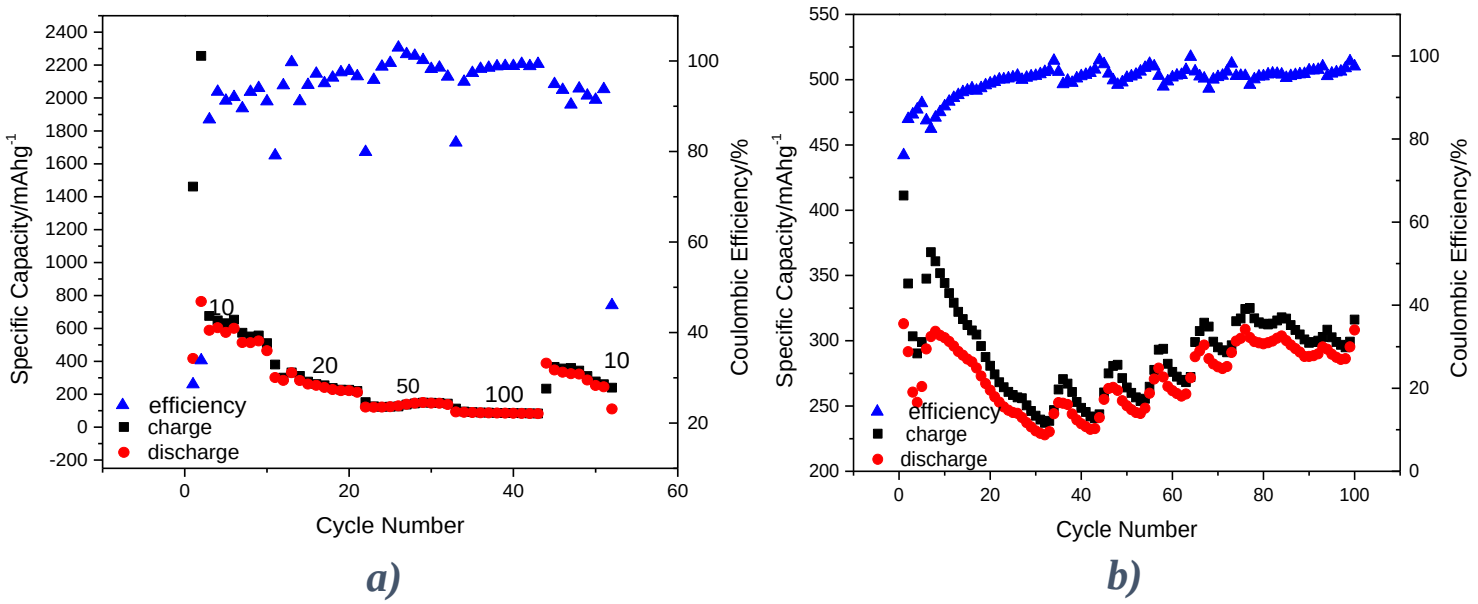

Figure 27.(a)Rate capability of MnHCF+AC-3M $ZnSO_4$+1M $MnSO_4$ with different(10,20,50,100 mAg^{-1}) current densities.(b) (a)long- term Stability test of MnHCF+AC-$ZnSO_4$+1M $MnSO_4$

The rate capability on MnHCF in $ZnSO_4$+1M $MnSO_4$ is shown in Fig.27(a), as the current density increases from 10 to 20,50 and 100 mAg^{-1}, the Zn/MnHCF+AC battery delivers max discharge capacities of 286, 115 and 104 mAg^{-1}, respectively, when the current density decreases back to 10 mAg^{-1}, it can be restored to a high capacity of 378 mAg^{-1}, indicating good reversibility.

The long- term stability is investigated at a current density of 50mAg^{-1}. In Fig 27(b)The initial discharge capacity of MnHC+AC is 295 $mAhg^{-1}$. the capacity decreases to 230 $mAhg^{-1}$ in the first 30 cycles, and then increases to almost 300 $mAhg^{-1}$ in the subsequent 70 cycles. All the noises in the curve are attributed to the change of temperature in the atmosphere of the lab.

3.4 CV and battery analysis of MnHCF and MnHCF+AC -3M Zn $(OTF)_2$

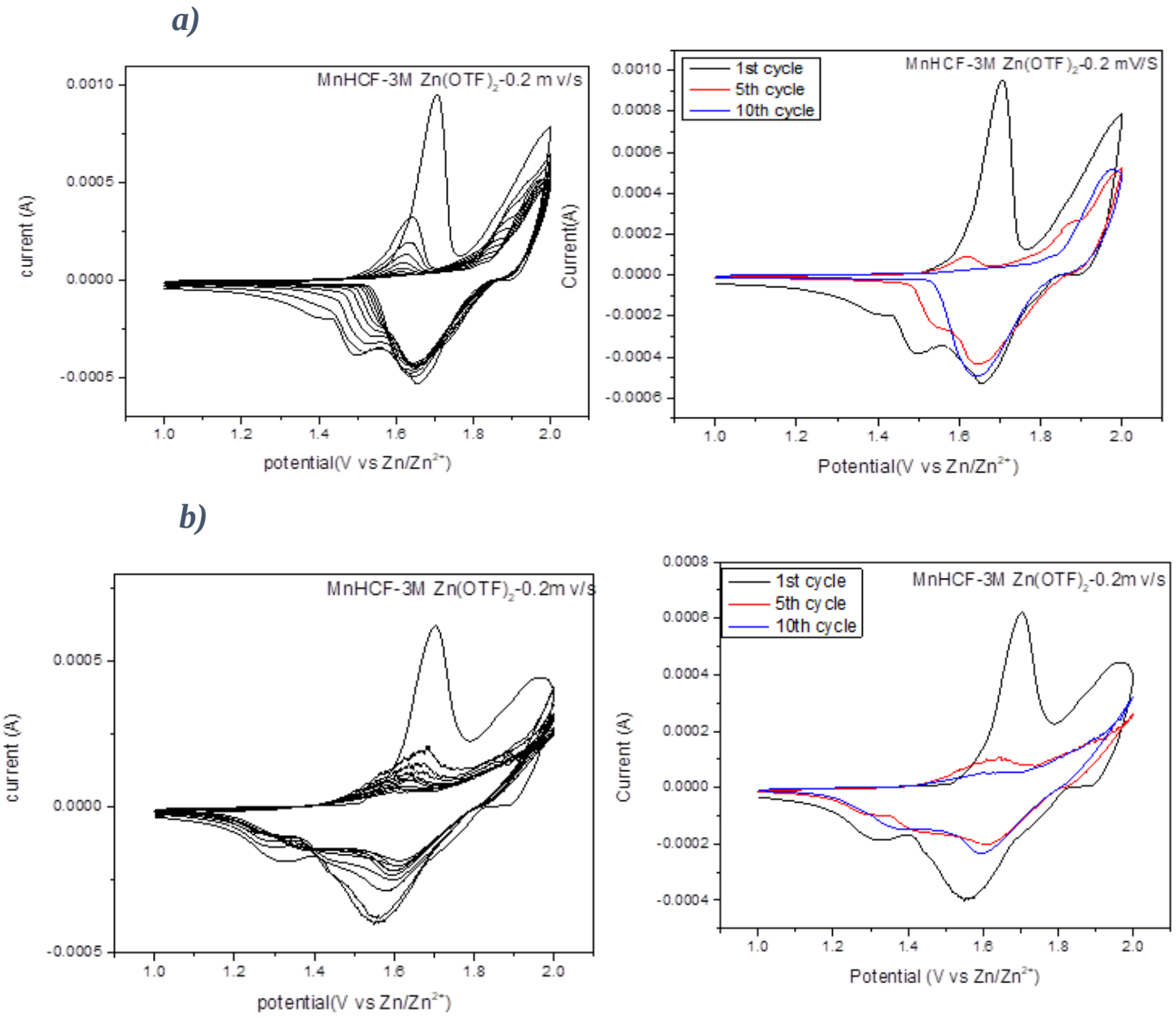

Figure 28. Cyclic voltammetry of MnHCF-3M $Zn(OTF)_2$electrolyte

As shown in figure 28 in 3M Zn (OTF)2 electrolyte, Cyclic voltammetry (CV) curves were recorded at 0.2 mV/s scan rates for 2 same samples to see if the results are the same or not, in the voltage range from 1 to 2 V. 2. The CV profile in the first cycle is slightly different from the following ones. For the first cycle in the first sample there are two oxidation peaks at around 1.71 V and 1.99 V and two reduction peaks at around 1.65 V and 1.90 V while in the 5th and 10th cycle there is only 1 weak oxidation and

reduction peak. for the second sample, Fig 28(b) for the first cycle there are 2 oxidation peaks at around 1.7 V and 1.97 V and two reduction peaks at around 1.55 V and 1.90 V. while in the 5th and 10th cycle there is only one weak oxidation and reduction peak.

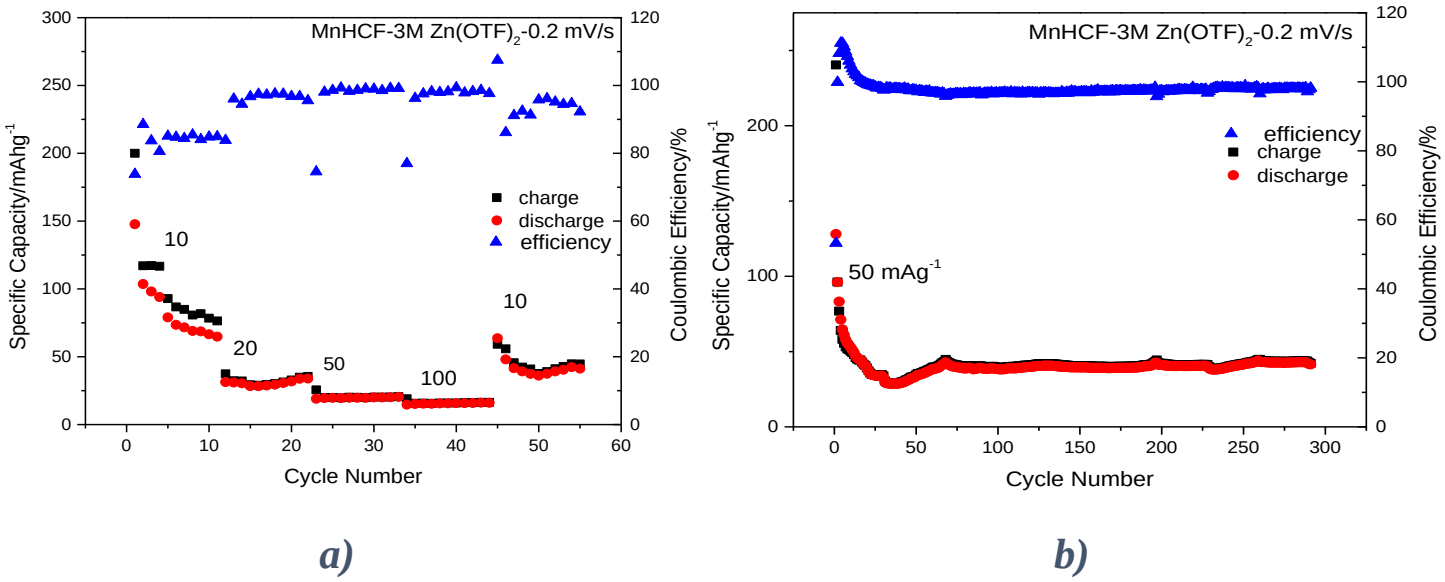

Figure 29. (a)Rate capability of MnHCF-3M $Zn(OTF)_2$ with different(10,20,50,100) current densities.(b) (a)long- term Stability test of MnHCF-$Zn(OTF)_2$

The rate capability on MnHCF in $Zn(OTF)_2$ is shown in Fig.29(a), as the current density increases from 10 to 20,50 and 100 mAg^{-1} , the Zn/MnHCF+AC battery delivers max discharge capacities of 78, 34 and 16 mAg^{-1} , respectively, when the current density decreases back to 10 mAg^{-1} , it can not be restored to a high capacity of 378 mAg^{-1}, which does not indicate good reversibility.

The long- term stability is investigated at a current density of 50mAg^{-1}. In Fig 29(b)The initial discharge capacity of MnHC is 81 $mAhg^{-1}$. the capacity decreases to 25 $mAhg^{-1}$ in the first 40 cycles, and then increases to almost 41 $mAhg^{-1}$ in the subsequent 260 cycles and shows a high stability. All the noises in the curve are attributed to the change of temperature in the atmosphere of the lab.

3.5 Comparison the performance of MnHCF and MnHCF-AC in 3M $ZnSO_4$ electrolyte

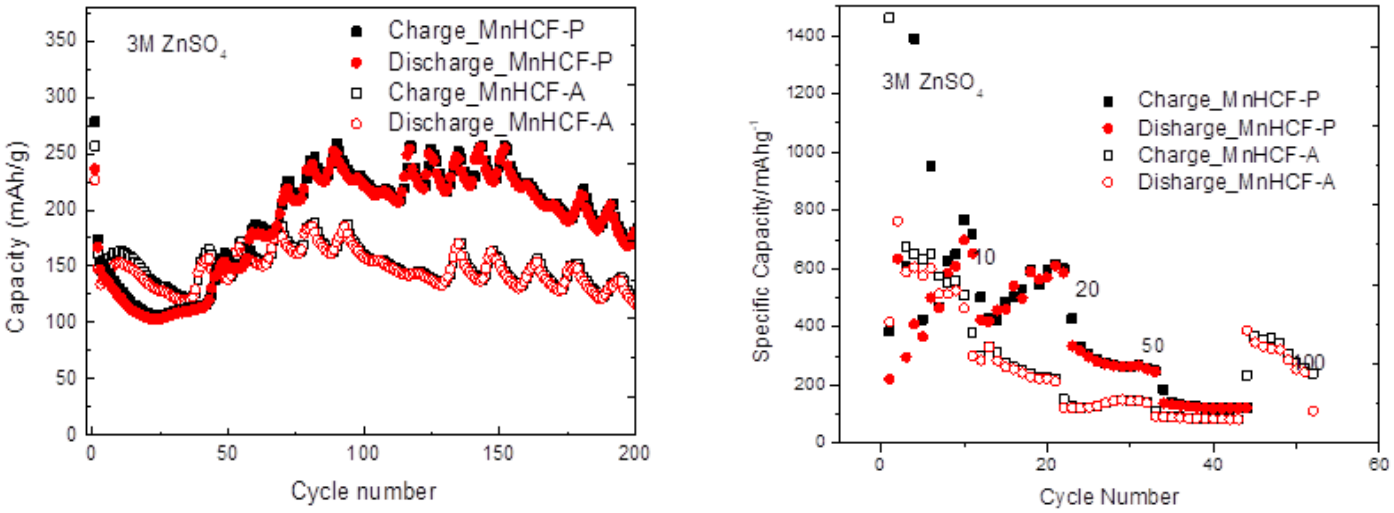

Figure 30. comparison the performance of MnHCF and MnHCF-AC in 3M $ZnSO_4$ electrolytre

As it is shown in Fig 30 in 3M $ZnSO_4$ electrolyte, the specific capacity of MnHCF-P was lower than MnHCF-A sample at the beginning 50 cycles, After 50 cycles, the specific capacity of MnHCF-P increased around to 250 mAh g-1. Different from the MnHCF-P sample, sample MnHCF-A keep specific capacity around 150 mAh g-1.

3.6 Comparison the performance of MnHCF and MnHCF-AC in 3M $ZnSO_4$ + 1M $MnSO_4$ electrolyte

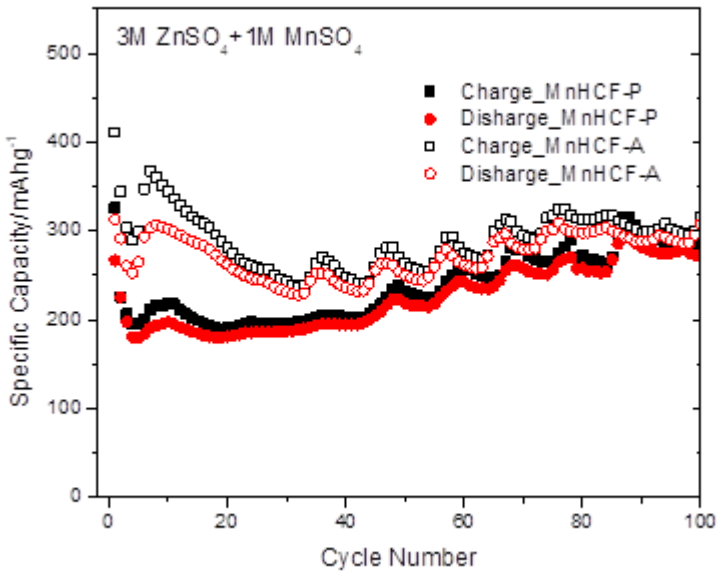

Figure 31.Comparison the performance of MnHCF and MnHCF-AC in 3M $ZnSO_4$+ 1M $MnSO_4$ electrolyte

As shown in Fig 31 in 3M $ZnSO_4$ +1M $MnSO_4$ electrolyte, the specific capacity of MnHCF-A was higher than MnHCF-A sample at the beginning, and also keep a quite stable value for 100 cycles.

3.7 Comparison the performance of MnHCF and MnHCF-AC in different electrolyte

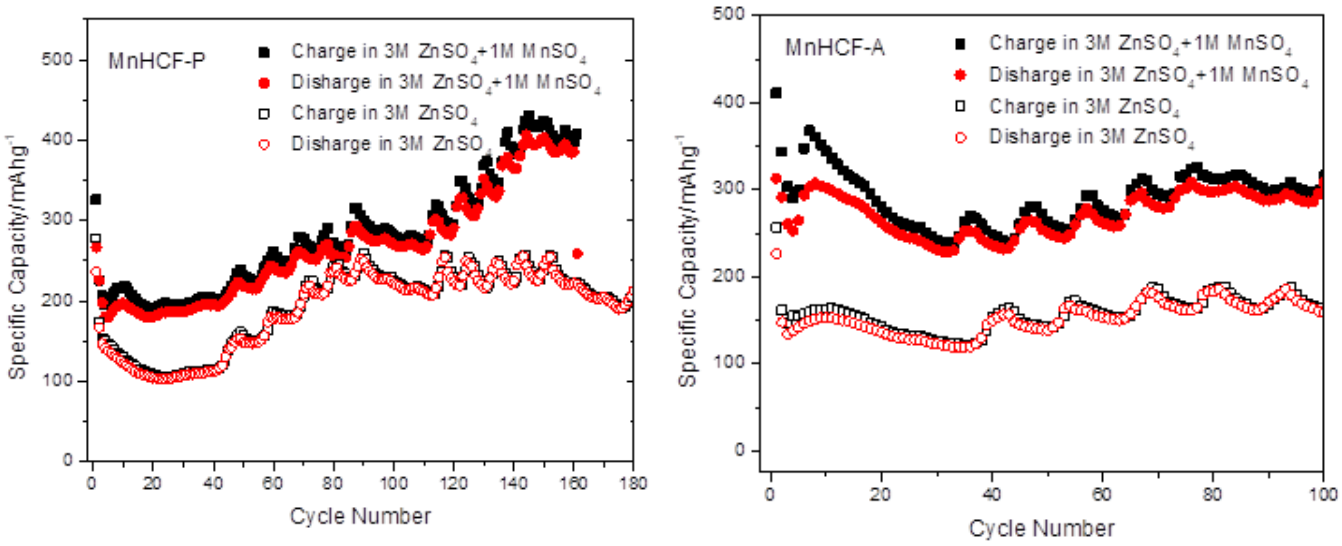

Figure 32.Comparison the performance of MnHCF and MnHCF-AC in different electrolytes

The comparison of electrochemical performance of MnHCF-P and MnHCF-A in 3M ZnSO4 and 3M $ZnSO_4$+1M $MnSO_4$ are Shown in Fig 32. A better electrochemical performance was observed in 3M $ZnSO_4$+1M $MnSO_4$ electrolyte. One reason might due to the addition of Mn^{2+} prohibited the dissolution of MnHCF sample. The detailed structure evolution information of MnHCF electrode will be studied later.

4. Conclusion

In this work, Prussian blue analogue -mangenase hexacyanoferrate (MnHCF) has been synthesized by simple co-precipitation method, and the as-prepared sample was characterized MP-AES. The obtained material MnHCF has the chemical formula of $Na_{1.98}Mn\ [Fe(CN)_6]_{0.7}$,and MnHCF+AC has the chemical formula of $Na_{2.17}Mn\ [Fe(CN)_6]_{0.72}$.

The as-prepared sample show good performance in electrochemical test. The sample was tested in aqueous system; we observed redox peaks of both $Fe^{3+/2+}$ and $Mn^{3+/2+}$ pairs from cyclic voltammetry curves. From the calculation result based on scan rate and current, we conclude that the capacity of battery is controlled by diffusion process. It indicates that the cationic ions (Zn^{2+}, Mg^{2+}) insert inside the crystal structure (A-site) during discharge process. It has been found that addition of chelating agents has led to the relative increase of sodium content which was confirmed by means of MP-AES technique.

The intrinsic non-toxicity, high reversibility and environmentally friendliness characterizing the family of PBAs make them ideal candidates as active materials for the positive electrodes of aqueous Zn-ion batteries. Moreover, their easy synthesis procedure is extremely appealing for their possible scaled-up production, in view of a commercialization of aqueous Zn-ion cells.

References

[1]. D. Sprake, Y.Vagapov. Housing Estate Energy Storage Feasibility for a 2050 Scenario. Conference:7th International Conference on Internet Technologies and Applications At: Wrexham, UK. DOI: 10.1109/ITECHA.2017.8101925.

[2].J.Song, L. Wang, Y.h.Lu, J. Liu, B.k. Guo, P.h. Xiao, J.-J. Lee, X.-Q. Yang, G. Henkelman,J. B. Goodenough. Removal of Interstitial H_2O in Hexacyanometallates for a Superior Cathode of a Sodium-Ion Battery. J. Am. Chem. Soc. 2015, 137, 2658-2664

[3]. M. S. WHITTINGHAM, Electrical Energy Storage and Intercalation Chemistry. Science,1976, Vol.192, Issue 4244, pp. 1126-1127

[4]. Keywords to understanding Sony Energy Devices- keyword 1991".

[5]. Monthly battery sales statistics. Machinery statistics released by the ministry of economy, trade and industry, March 2011.

[6]. K. C. Kam, M. M. Doeff. Electrode Materials for Lithium Ion Batteries. Material Matters, 2012, 7, 4.

[7]. A. Mishra, A. Mehta, S. Basu, S. J. Malode, N. P. Shetti , S. S. Shukla, M. N. Nadagouda, T.M. Aminabhavi. Electrode materials for lithium-ion batteries. Materials Science for Energy Technologies, 2018, 1, 182-187.

[8].T. Matsuda, M. Takachi, Y. Moritomo. A sodium manganese ferrocyanide thin film for Na- ion batteries. Chem. Commun., 2013, 49, 2750-2752.

[9]. Battery energy storage. White paper. suschem battery energy storage white paper

[10]. R. D. Shannon, Revised effective ionic radii and systematic studies of interatomic distances in halides and chalcogenides,Acta Cryst. (1976). A32,751-767.

[11]. J.Y. Hwang, S.T. Myung, Y.K. Sun. Recent Progress in Rechargeable Potassium Batteries. Adv. Funct. Mater. 2018, 28, 1802938.

[12]. T. R. Juran, J. Young and M. Smeu, J. Phys. Chem. C, 2018, 122, 8788‑8795.

[13]. J. Lee, J. B. Ju, W. I. Cho, B. W. Cho and S. H. Oh,Electrochim. Acta, 2013, 112, 138‑143.

[14]. C. Xu, B. Li, H. Du and F. Kang, Angew. Chem., Int. Ed., 2012, 51, 933‑935.

[15]. S. H. Kim and S. M. Oh, J. Power Sources, 1998, 72, 150‑158.

[16]. C. Wei, C. Xu, B. Li, H. Du and F. Kang, J. Phys. Chem. Solids, 2012, 73, 1487‑

1491.

[17]. M. H. Alfaruqi, V. Mathew, J. Gim, S. Kim, J. Song, J. P. Baboo, S. H. Choi and J. Kim, Chem. Mater., 2015,27, 3609‑3620.

[18]. S. Islam, M. H. Alfaruqi, V. Mathew, J. Song, S. Kim, S. Kim, J. Jo, J. P. Baboo, D. T. Pham, D. Y. Putro, Y.-K. Sun and J. Kim, J. Mater. Chem. A, 2017, 5, 23299‑23309.

[19]. Q. Feng, H. Kanoh, Y. Miyai and K. Ooi, Chem. Mater., 1995, 7, 1722‑1727.

[20]. J. C. Knight, S. Therese and A. Manthiram, J. Mater. Chem. A, 2015, 3, 21077‑21082.

[21]. N. Zhang, F. Cheng, Y. Liu, Q. Zhao, K. Lei, C. Chen, X. Liuand J. Chen, J. Am. Chem. Soc., 2016, 138, 12894‑12901.

[22]. H. Zhang, J. Wang, Q. Liu, W. He, Z. Lai, X. Zhang, M. Yu, Y. Tong and X. Lu, Energy Storage Mater., 2018, 21, 154‑161.

[23]. N. Qiu, H. Chen, Z. Yang, S. Sun and Y. Wang, Electrochim. Acta, 2018, 272, 154‑160.

[24]. C. Zhu, G. Fang, S. Liang, Z. Chen, Z. Wang, J. Ma, H. Wang, B. Tang, X. Zheng and J. Zhou, Energy Storage Mater., 2019, DOI: 10.1016/j.ensm.2019.07.030.

[25]. B. Jiang, C. Xu, C. Wu, L. Dong, J. Li and F. Kang, Electrochim. Acta, 2017, 229, 422‑428.

[26]. M. Sun, D. S. Li, Y. F. Wang, W. L. Liu, M. M. Ren, F. G.Kong, S. J.Wang, Y. Z. Guo and Y. M. Liu, ChemElectroChem, 2019, 6, 2510‑2516.

[27]. J. Hao, J. Mou, J. Zhang, L. Dong, W. Liu, C. Xu and F. Kang, Electrochim. Acta 2018, 259, 170‑178.

[28]. V. Soundharrajan, B. Sambandam, S. Kim, V. Mathew, J. Jo,S. Kim, J. Lee, S. Islam, K. Kim, Y.-K. Sun and J. Kim, ACS Energy Lett., 2018, 3, 1998‑2004.

[29]. X. Yao, Y. Zhao, F. A. Castro and L. Mai, ACS Energy Lett., 2019, 4, 771‑778.

[30]. B. Tang, J. Zhou, G. Fang, S. Guo, X. Guo, L. Shan, Y. Tang and S. Liang, J. Electrochem. Soc., 2019, 166, A480‑A486.

[31]. T. Wei, Q. Li, G. Yang and C. Wang, J. Mater. Chem. A, 2018, 6, 8006‑8012.

[32]. J. Ding, Z. Du, L. Gu, B. Li, L. Wang, S. Wang, Y. Gong and S. Yang, Adv. Mater., 2018, 30, 1800762.

[33]. L. Shan, J. Zhou, W. Zhang, C. Xia, S. Guo, X. Ma, G. Fang, X. Wu and S.

Liang, Energy Technol., 2019, 7, 1900022.
[34]. F. Liu, Z. Chen, G. Fang, Z. Wang, Y. Cai, B. Tang, J. Zhou and S. Liang, Nano-Micro Lett., 2019, 11, 25.
[35]. M. Ware, "Prussian Blue: Artists' Pigment and Chemists' Sponge," Journal of Chemical Education, vol. 85, no. 5, p. 612, 2008.
[36]. N. R. De Tacconi, K. Rajeshwar, and R. O. Lezna, "Metal hexacyanoferrates: Electrosynthesis, in situ characterization, and applications," *Chemistry of Materials*, vol. 15, no. 16, pp. 3046–3062, 2003.
[37]. H. J. Buser, D. Schwarzenbach, W. Petter, and a. Ludi, "The crystal structure of Prussian Blue: Fe4[Fe(CN)6]3.xH2O," *Inorganic Chemistry*, vol. 16, no. 11, pp. 2704–2710, 1977.
[38]. M. Giorgetti, "Review Article A Review on the Structural Studies of Batteries and Host Materials by X-Ray Absorption Spectroscopy," *ISRN Materials Science*, vol. 2013, 2013.
[39]. M. Giorgetti, D. Tonelli, M. Berrettoni, G. Aquilanti, and M. Minicucci, "Copper hexacyanoferrate modified electrodes for hydrogen peroxide de- tection as studied by X-ray absorption spectroscopy," *J. Solid State Elec- trochem.*, vol. 18, no. 4, pp. 965–973, 2013.
[40]. L. Guadagnini, D. Tonelli, and M. Giorgetti, "Improved performances of elec- trodes based on Cu^{2+}-loaded copper hexacyanoferrate for hydrogen peroxide detection," *Electrochimica Acta*, vol. 55, no. 17, pp. 5036–5039, 2010.
[41]. M. Giorgetti, L. Guadagnini, D. Tonelli, M. Minicucci, and G. Aquilanti, "Structural characterization of electrodeposited copper hexacyanoferratefilms by using a spectroscopic multi-technique approach," *Physical ChemistryChemical Physics*, vol. 14, no. 16, p. 5527, 2012.
[42]. H. Tokoro and S.-i. Ohkoshi, "Novel magnetic functionalities of Prussian blueanalogs.," *Dalton transactions (Cambridge, England : 2003)*, vol. 40, no. 26, pp. 6825–6833, 2011.
[43]. J. Jiménez-Gallegos, J. Rodríguez-Hernández, H. Yee-Madeira, andE. Reguera, "Structure of porous copper prussian blue analogues: Natureof their high H2 storage capacity," *Journal of Physical Chemistry C*, vol. 114, no. 11, pp. 5043–5048, 2010.
[44]. S. Liu, G. L. Pan, G. R. Li, and X. P. Gao, "Copper hexacyanoferrate nanoparticles as cathode material for aqueous Al-ion batteries," *J. Mater. Chem.*

A, vol. 3, no. 3, pp. 959–962, 2014.

[45]. C. D. Wessells, R. a. Huggins, and Y. Cui, "Copper hexacyanoferrate batteryelectrodes with long cycle life and high power.," *Nature Commun.*, vol. 2,p. 550, 2011.

[46]. J. P. Souza and D. R. Silvestrini, "Direct Preparation and Characterization of Copper Pentacyanonitrosylferrate Nanoparticles," *Journal of nanomaterials*, vol. 2015, 2015.

[47]. A. B. Nikolskii, N. B. Batalova, and Y. I. Dyachenko, "Study of the nature of M-NO bond in nitroso complexes," *Teoeticheskaya i Eksperimental'naya Khimiya*, vol. 15, no. 2, pp. 153–156, 1979.

[48]. Brown, "Nitrogen and Oxigen bonded Nitrosyl. Metal coplexes of the nitroprusside ion.," *Inorg. Chem.*, vol. 14, no. 10, pp. 2582–2584, 1975.

[49]. M. D. Carducci, M. R. Pressprich, and P. Coppens, "Diffraction studies of photoexcited crystals: Metastable nitrosyl-linkage isomers of sodium nitroprusside," *Journal of the American Chemical Society*, vol. 119, no. 11, pp. 2669–2678, 1997.

[50]. P. Coppens, I. Novozhilova, and A. Kovalevsky, "Photoinduced linkage isomers of transition metal nitrosyl compounds and related complexes," *Chem-ical Reviews (Washington, D. C.)*, vol. 102, no. 4, pp. 861–883, 2002.

[51]. A. Gomez, J. Rodriguez-Hernandez, and E. Reguera, "Unique coordination in metal nitroprussides: The structure of Cu[Fe(CN)5NO].2H2O and Cu[Fe(CN)5NO]," *J. Chem. Crystallogr.*, vol. 34, pp. 893–903, Dec. 2004.

[52]. A. C. de Sá, L. L. Paim, U. D. O. Bicalho, and D. R. do Carmo, "Determina- tion of N-acetylcysteine by cyclic voltammetry using modified carbon paste electrode with copper nitroprusside adsorbed on the 3-aminopropylsilica," *In- ternational Journal* of Electrochemical Science, vol. 6, no. 9, pp. 3754–3767, 2011.

[53]. A. Eftekhari. Potassium secondary cell based on Prussian blue cathode. Journal of Power Sources, 2004, 126, 221-228.

[54]. O. Makowski, J. Stroka, P. J. Kulesza, M. A. Malik, Z. Galus. Electrochemical identity of copper hexacyanoferrate in the solid-state:evidence for the presence and redox activity of both iron and copper ionic sites. Journal of Electroanalytical Chemistry, 2002, 532, 157-164.

[55]. A. Dostal. Festko¨rperreaktionen an metallhexacyanometallat -modifiziertem

Elektroden. Dr.Diss. Math. Fak. I der Humboldt-Universita¨t zu Berlin (1998).

[56]. C. D. Wessells, S.V. Peddada, R. A. Huggins,Y. Cui. Nickel Hexacyanoferrate NanoparticleElectrodes for Aqueous Sodium and Potassium Ion Batteries. Nano Lett., 2011, 11, 5421-5425.

[57].A. Mullaliu, G. Aquilanti, P. Conti, J. R. Plaisier, M. Fehse, L. Stievano, M. Giorgetti. Copper Electroactivity in Prussian Blue-Based Cathode Disclosed by Operando XAS. J. Phys. Chem. C, 2018, 122, 15868-15877.

[58]. A. Mullaliua, M. T. Sougrati, N. Louvain, G. Aquilanti, M. L. Doublet, L. Stievano, M. Giorgetti. The electrochemical activity of the nitrosyl ligand in copper nitroprusside: a new possibleredox mechanism for lithium battery electrode materials? Electrochimica Acta, 2017, 257, 364-371.

[59]. Kevin Hurlbutt, Samuel Wheeler, Isaac Capone, Mauro Pasta, "Prussian Blue Analogs as Battery Materials," vol. 2, p. 1950–1960, 2018.

[60]. H.J. Buser, A. Ludi, D. Schwarzenbach and W. Petter., "The crystal structure of Prussianblue: Fe4[Fe(CN)6]3•xH2O," *Inorg. Chem,* vol. 16, pp. 2704-2710, 1977

[61]. Y.-M. Chiang, Y.-I. Jang, H. Wang, B. Huang, D.R. Sadoway and P. Ye., "Synthesis of LiCoO2 by decomposition and intercalation of hydroxide," *J. Electrochem. Soc.,* no.

[62]. M. Takachi, T. Matsuda and Y. Moritomo., "Redox reactions in prussian blue analoguesagainst Li concentration," *J. Appl. Phys.,* no. 52, p. 9, 2013.

[63]. Y. Moritomo, K. Wakaume, M. Takachi, X.H. Zuo and H. Kamioka., "Li^+ intercalation of manganese hexacyanoferrate as investigated by in situ valence-differential absorptionspectroscopy.," *J. Appl. Phys,* vol. 52, p. 17, 2013.

[64]. Xiaomin Yan, Yang Yang, Ershuai Liu, Liqi Sun, Hong Wang, Xiao-Zhen Liao, Yushi He, Zi-Feng Ma, "Improved cycling performance of prussian blue cathode for sodium ion batteries by controlling operation voltage range," *Electrochimica Acta,* vol. 225, pp.235-242, 2017.

[65]. L. Wang, Y. H. Lu, J. Liu, M. W. Xu, J. G. Cheng, D. W. Zhang,J. B. Goodenough,

Angew. Chem., Int. Ed., no. 52, p. 1964, 2013.

[66]. W. J. Li, S. L. Chou, J. Z. Wang, J. L. Wang, Q. F. Gu, H. K. Liu, S. X. Dou, *NanoEnergy,* vol. 200, p. 13, 2015.

[67]. J. Song, L. Wang, Y. H. Lu, J. Liu, B. K. Guo, P. H. Xiao, J. J. Lee,X. Q. Yang, G.Henkelman, J. B. Goodenough, *J. Am. Chem. Soc.,* vol. 137, p. 2658, 2015.

[68].Y. Tang, W. Zhang, L. Xue, X. Ding, T. Wang, X. Liu, J. Liu, X. Li and Y. Huang., "Polypyrrole-promoted superior cyclability and rate capability of NaxFe[Fe(CN)6] cathodes for sodium-ion batteries," *Journal of Materials Chemistry A*, vol. 4, pp. 6036-604, 2016.

[69].Y. You, X.-L. Wu, Y.-X. Yin and Y.-G. Guo., "High-quality Prussian blue crystals assuperior cathode materials for room-temperature sodium-ion batteries," *Energy & Environmental Science*, vol. 7, pp. 1643-1647, 2014

[70]. W. Li, J.R. Dahn, D.S. Wainwright, Rechargeable lithium batteries with aqueous electrolytes, Science 264 (2016) 1115–1118.

[71].M.H. Lee, S.J. Kim, D. Chang, J. Kim, S. Moon, K. Oh, K.Y. Park, W.M. Seong,H. Park, G. Kwon, B. Lee, K. Kang, Toward a low-cost high-voltage sodium aqueous rechargeable battery, Mater. Today 29 (2019) 26–36, doi:10.1016/j. mattod.2019.02.004.

[72].L. Wang, Y. Lu, J. Liu, M. Xu, J. Cheng, D. Zhang, J.B. Goodenough, A superior low-cost cathode for a Na-Ion battery, Angew. Chem. Int. Ed. 52 (2013) 1964– 1967,

[73]A. Eftekhari, Potassium secondary cell based on Prussian blue cathode, J. Power Sources 126 (2004) 221–228

[74].Y. Mizuno, M. Okubo, E. Hosono, T. Kudo, K. Oh-Ishi, A. Okazawa, N. Kojima, R. Kurono, S.I. Nishimura, A. Yamada, Electrochemical Mg^{2+} intercalation into a bimetallic CuFe Prussian blue analog in aqueous electrolytes, J. Mater. Chem. A 1 (2013) 13055–13059

[75].C. Xu, B. Li, H. Du, F. Kang, Energetic zinc ion chemistry: the rechargeable zinc ion battery, Angew. Chem. Int. Ed. 51 (2012) 933–935, doi:10.1002/anie. 201106307.

[76].N. Kuperman, P. Padigi, G. Goncher, D. Evans, J. Thiebes, R. Solanki, High performance Prussian Blue cathode for nonaqueous Ca-ion intercalation battery, J. Power Sources 342 (2017) 414–418

[77].W.J. Li, S.L. Chou, J.Z. Wang, Y.M. Kang, J.L.Wang, Y.Liu, Q.F. Gu, H.K. Liu,S.X. Dou, Facile method to synthesize na-enriched $Na^{1+}xFeFe(CN)_6$ frame- works as cathode with superior electrochemical performance for sodium-ion batteries, Chem. Mater. 27 (2015) 1997–2003, doi:10.1021/cm504091z.

[78].Y. Hu, D. Ye, B. Luo, H. Hu, X. Zhu, S. Wang, L. Li, S. Peng, L. Wang, A binder-free and free-standing cobalt Sulfide@Carbon nanotube cathode mate- rial for Aluminum-ion batteries, Adv. Mater. 30 (2018) 1–6

[79].R. Trócoli, F.La Mantia, An aqueous zinc-ion battery based on copper hexa-cyanoferrate, ChemSusChem 8 (2015) 481–485.

[80].B. Tang, L. Shan, S. Liang, J. Zhou, Issues and opportunities facing aqueous zinc-ion batteries, Energy Environ. Sci. 12 (2019) 3288–3304

[81].J. Shin, J. Lee, Y. Park, J.W. Choi, Aqueous zinc ion batteries: focus on zinc metal anodes, Chem. Sci. 11 (2020) 2028–2044

[82]. F. Wan, L. Zhang, X. Dai, X. Wang, Z. Niu and J. Chen, Nat.Commun., 2018, 9, 1656.

[83]. R. Tro ´ coli, G. Kasiri and F. La Mantia, J. Power Sources,2018, 400, 167‑171.

[84]. F. Wang, O. Borodin, T. Gao, X. Fan, W. Sun, F. Han,A. Faraone, J. A. Dura, K. Xu and C. Wang, Nat. Mater.,2018, 17, 543‑549.

[85].C. Zhang, J. Holoubek, X. Wu, A. Daniyar, L. Zhu, C. Chen,D. P. Leonard, I. A. Rodrı ´ guez-Pe ´ rez, J.-X. Jiang, C. Fang and X. Ji, Chem. Commun., 2018, 54, 14097‑14099.

[86]. A. Bani Hashemi, G. Kasiri and F. La Mantia, Electrochim.Acta, 2017, 258, 703‑708.

[87]. A. Naveed, H. Yang, J. Yang, Y. Nuli and J. Wang, Angew. Chem., Int. Ed., 2019, 58, 2760‑2764.

[88]. Q. Zhang, J. Luan, L. Fu, S. Wu, Y. Tang, X. Ji and H. Wang, Angew. Chem., Int. Ed., 2019, DOI: 10.1002/anie.201907830.

[89]. K. Boto, Electrodeposition Surf. Treat., 1975, 3, 77‑95.

[90]. Z. Hou, X. Zhang, X. Li, Y. Zhu, J. Liang and Y. Qian, J. Mater. Chem. A, 2017, 5, 730‑738.

[91].S.Abdoun.Electrochemical methods of analysis. https://www.slideshare.net/SihamAbdallaha/electrochemical-method-of-analysis-31352857.

[92].R.S. Nicholson. Theory and Application of Cyclic Voltammetry for Measurement ofElectrode Reaction Kinetics. Anal. Chem., 1965, 37,11, 1351-1355.

[93]. Y. H. Lu, L. Wang, J. G. Cheng, J. B. Goodenough. Prussian blue: a new framework of electrode materials for sodium batteries. Chem. Commun., 2012, 48, 6544.

[94].C. D. Wessells, et al. Copper hexacyanoferrate battery electrodes with long

cycle life andhigh power. Nat. Commun.2011, 2, 550. doi: 10.1038/ncomms1563.

[95]. Balasubramanian, M., Sun, X., Yang, X.Q., McBreen, J., "In Situ X-Ray Diffraction and X-Ray Absorption Studies of High-Rate Lithium-Ion Batteries.," J. Power Sources., no. 92, pp. -8, 2001.

[95]. Angelo Mullaliu, Jakob Asenbauer, Giuliana Aquilanti, Stefano Passerini, Marco Giorgetti., "Highlighting the Reversible Manganese Electroactivity in Na-Rich Manganese Hexacyanoferrate Material for Li- and Na-Ion Storage," Small Methods Journal, 2020.

[96]. J. Song, L. Wang, Y.h.Lu, J. Liu, B.k. Guo, P.h. Xiao, J.-J. Lee, X.-Q. Yang, G. Henkelman, J. B. Goodenough., "Removal of Interstitial H2O in Hexacyanometallatesfor a Superior Cathode of a Sodium-Ion Battery.," J. Am. Chem. Soc., vol. 137, pp. 2658- 2664, 2015.

Appendix A

How to choose which concentration of $MnSO_4$ is better to continue the tests?

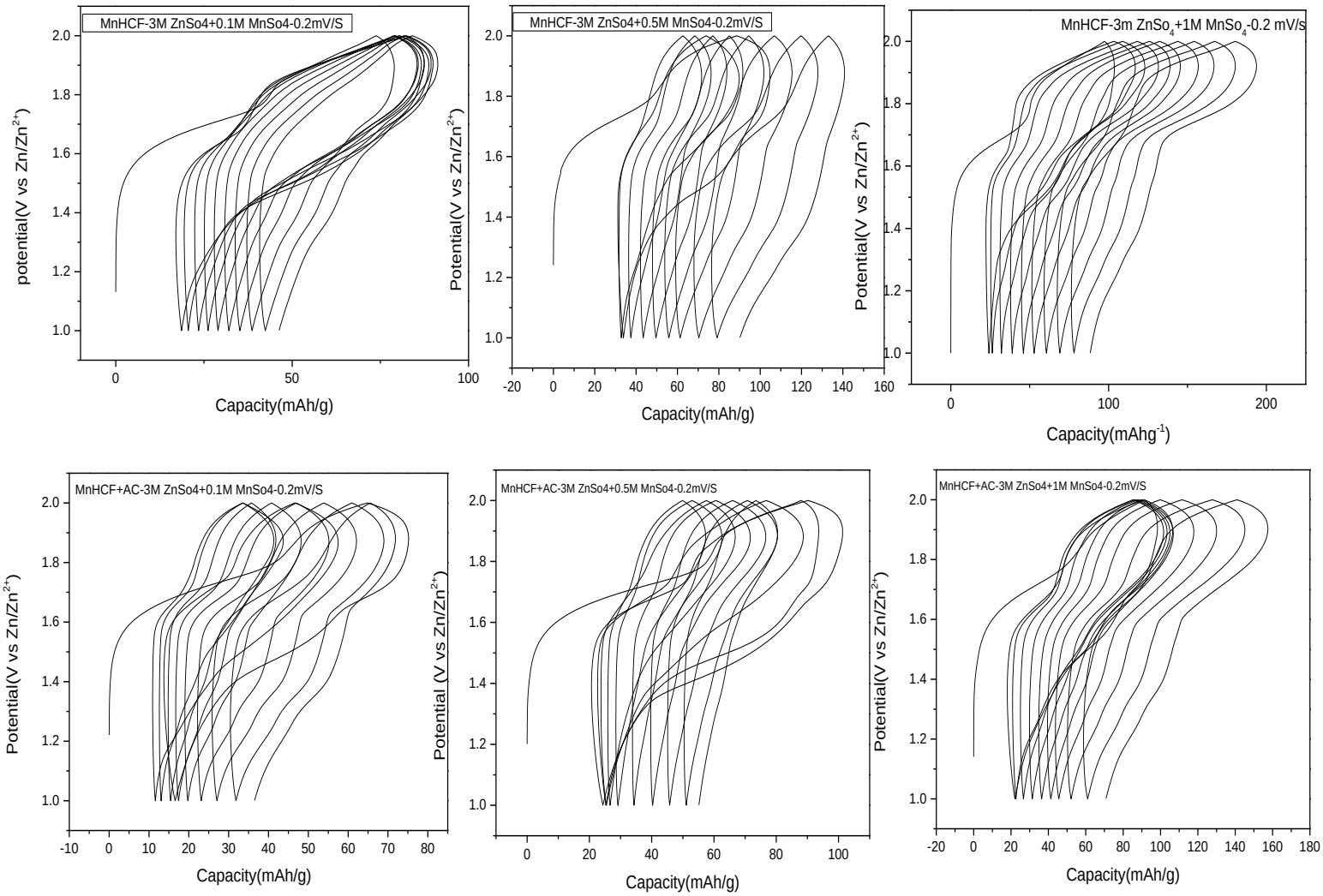

Capacity calculation based on cyclic voltammetry for MnHCF and MnHCF+AC based on integration

appendix B

Capacity calculation based on cyclic voltammetry

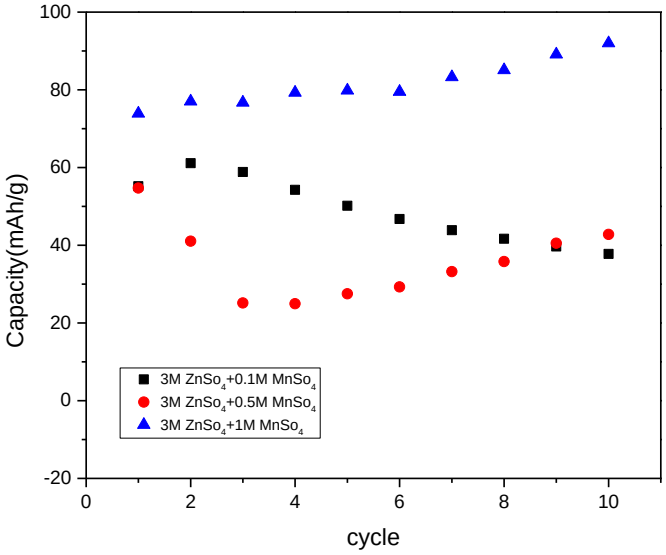

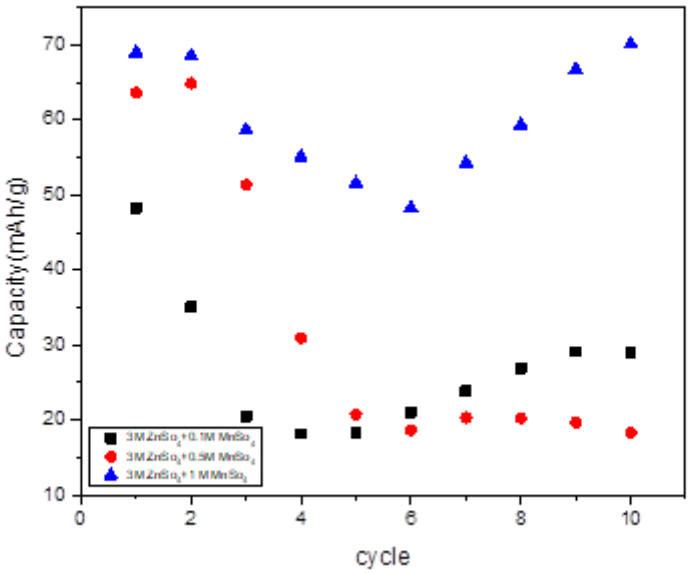

Acknowledgement

I want to thank my supervisor, Professor Marco Giorgetti, who always supported and guided me throughout my second year in University of Bologna. Thank you for giving me a chance to work and get new experience in the electrochemical field, and inspire me to continue my scientific career.

In addition, I want to thank Min Li, who was always so kind and patient in laboratory and really helped me in my electrochemical research. Separate thank to my colleague Mariam Maisuradze who was literally every day by my side.

At last, I want to say thanks to my family: my husband, my parents and my sisters who never understand what specifically I do in science but always encourage me to follow my dreams.